Acoustic Emission Tomography Based on Lasso Regression

(ラッソ回帰に基づく AE トモグラフィ法による土木構造物の非破壊検査)

January 2023

Civil engineering Major

Graduate School of Science and Technology

Doctoral Course

Nihon University

QIAO XIN

CONTENTS

1 INTRODUCTION

1.1 Background

With the rapid development of social and economic development, the scale of infrastructure is expanding simultaneously, and the number of enormous frustrations increasing, such as buildings, highways, bridges, and tunnels. As we know, concrete is the world's most extensive and versatile construction material. Due to economic applicability and ease of forming, concrete has become an irreplaceable building material widely used in transportation, water conservancy, and industrial and public infrastructure facilities. As concrete structures become aged and under the damage of natural disasters such as earthquakes, various defects inside the structure that are difficult to identify with the naked eye will appear to varying degrees. These defects may affect the structure's load-bearing capacity, with the possibility of insecurity. Performance assessment and quality inspection of aging concrete structures is an urgent issue for the civil engineering community. The non-destructive testing technology for concrete structures can reflect the localization and measurement of defects within the structure while achieving its internal defects, which provides a fast and accurate basis for concrete restoration. Moreover, non-destructive testing for concrete structures in advance provides warning for safety, offers time and chance to find and eliminate the hidden dangers of safety quickly, and protects people's lives and property. While the maintenance and reinforcement treatment for defective parts ensure the structures stay healthy and safe and extend service life. Therefore, conducting a series of comprehensive safety assessments has an irreplaceable and essential role.

1.2 Classification of non-destructive testing

Non-destructive testing of concrete structures is a technology that detects internal defects in a way that does not affect or damage the structure itself and then evaluates its serviceability. The economic losses caused by the durability of concrete structures worldwide are enormous. Many reinforced concrete structures fail prematurely for various reasons, including failing to reach their intended service life and having to be reinforced and repaired in advance. Therefore, assessing the durability of concrete structures is a vital problem that needs to be solved in building maintenance and renovation work. It is possible to recognize the exterior of the structure superficially by the naked eye, but almost impossible to quantify the damage inside the structure. Consequently, non-destructive testing is significant. Non-destructive testing (NDT) technology has been widely used in agricultural products testing, aviation, materials science, civil engineering, mechanical manufacturing, metallurgy, electric power, and other industries[1]-[6]. The generally classify for concrete non-destructive testing includes infrared testing technology, radar wave testing technology, impact echo testing technology (IE), ultrasonic rebound testing

technology, ultrasonic testing technology, acoustic emission testing technology, and acoustic emission (AE) tomography etc.

1.2.1 Infrared testing technology

The thermal imaging technique is known as infrared testing technology. The thermal conductivity of concrete serves as the foundation for most concrete testing equipment. If the concrete specimen has flaws, involving a heat source will cause a change in thermal conductivity. Meanwhile, a precise temperature distribution will develop on the concrete specimen's surface. The energy emitted by the received concrete specimen causes the infrared detector to create a contour heating figure. If the concrete specimen has flaws, each temperature gradient variation will be seen in the contour heating figure. The surface and underlying structure are often examined using the infrared testing method. The fault's size and depth considerably impact the testing result, as do the heating source, heating period, and ambient conditions. The external environment also takes into consideration like sunshine, wind, dust that scatters the absorption of the atmosphere, etc. The duration of the heat source's application to the concrete when infrared detection is used significantly impacts the test findings. The temperature of the defective and non-defective parts is almost the same when the heating source is used briefly. The contour heating figure makes it difficult to see the flaws in the concrete. On the other hand, if the heat source is provided for an extended period, the temperature of the concrete will increase throughout. Consequently, the detection result will differ significantly from the actual condition. Overall, the external environment and testing equipment have relatively high criteria for infrared testing technology. This technology is typically only possible in a laboratory setting, significantly restricting its use in concrete[7]-[8].

1.2.2 Radar wave testing technology

The variation in electromagnetic performance across various media forms is the foundation of the radar wave detection principle. The radar antenna's electromagnetic wave penetrates the object's interior after passing through its surface. The electromagnetic wave will then be reflected at the interface of the various dielectric constants. Finally, a radar image is created using specialized software to process the electromagnetic wave that the radar antenna reflects. This approach has a good detection depth, excellent spatial resolution, and a natural imaging result. Since it tests both the forms and the depth of the items, this non-destructive testing technique is now widely employed. Radar wave testing technology is extensively employed in geological exploration, civil engineering, agriculture, and other disciplines. However, its employment in reinforced concrete buildings is still uncommon due to particular circumstances. Electromagnetic waves are more intensely reflected and refracted when they come into contact with steel, cavities, and cracks because the dielectric constant of the sand, cement, and stone that makeup concrete differs somewhat from steel and air. Because steel bars are very sensitive to electromagnetic radiation, their detection rate is exceptionally high. The steel bar has a shielding effect and

impedes the further propagation of electromagnetic waves in the concrete when embedded inside it. The precision of radar wave testing equipment is additionally constrained by concrete's water content and radar antenna shielding[9]-[11].

1.2.3 Impact echo(IE) testing technology

The impact echo testing technique was developed in the 1980s[12]. It is common practice to evaluate concrete structures for thickness, internal flaws, depth of surface apertures, and fractures. Due to the elastic impact, a stress wave will be generated by impacting hammer strike on the concrete surface. The stress wave will be reflected as it travels through the concrete structure and comes into contact with an external interface or flaw. The receiving sensors pick up the reflected echo close to the impact location, and the results is evaluated by the received echo in the time domain or frequency domain. It is possible to determine the depth of the defect or the thickness of the concrete structure. The following are some benefits of using this testing method: the stress wave's instantaneous impact frequency is typically low; the wave attenuation is minimal when it travels through concrete, allowing it to travel deeper; and it is less sensitive to the internal aggregate and structural characteristics of the concrete[13]. Additionally, the specimen's surface roughness and flatness are unnecessary for this testing approach. Impact echo (IE) testing equipment has produced concrete quality evaluation findings. However, it is still challenging to quantify interior concrete flaws with IE testing technology[14]-[15].

1.2.4 Ultrasonic rebound testing technology

One of the non-destructive testing methods, ultrasonic rebound testing, was created in the 1960s[16]. The approach is used to gauge the strength of concrete. The ultrasonic rebound method was combined with ultrasonic and rebounding techniques. The heavy hammer used in the rebound technique is spring-driven and strikes the concrete specimen's surface. The strength of the concrete surface is determined by comparing the distance traveled by the heavy hammer on its rebound to the spring's starting length. There is a distinct correlation between concrete's compactness and strength; as ultrasonic waves travel through a concrete specimen, their speed reflects the concrete's density and compactness. The concrete rebound value is initially determined using the ultrasonic rebound method using rebound method (surface hardness). Finally, based on the link between rebound value, sound velocity, and concrete strength, calculate the ultrasonic wave propagation speed in concrete using the ultrasonic technique. Because concrete composition varies depending on location, it is required to identify the matching unique or regional strength measurement curve. However, many external elements, such as cement quality, ambient temperature, different additives, etc., readily affect the concrete strength measuring curve[17].

1.2.5 Ultrasonic testing technology

Leslie and Cheesman proposed ultrasonic testing for concrete and Jones in the late 1940s and early 1950s[18]. Early research on ultrasonic concrete testing focused primarily on the strength of the concrete, attenuation level, and speed of ultrasonic wave propagation. The following features of ultrasonic inspection are mainly involved: the depth of concrete cracks, the strength of the concrete, intelligence, quick detection of concrete defects, quantitative research on internal concrete defects, imaging study on an internal concrete structure, etc. Various structural flaws, such as voids, honeycombs, and inconsistent surfaces, may appear during the concrete pouring process. When the concrete construction is anomalous during the test, some phenomena (such as emission, refraction, and scattering) will manifest themselves. When the probe picks up reflected or refracted signals at the concrete interface, time domain or frequency domain data might be used to examine interior structures. The transmitting probe is typically placed on the concrete's detection surface for ultrasonic concrete testing. The receiving probe is then placed on the same or a different detection surface as the transmitting probe to receive ultrasonic waves. The ultrasonic waves are then used to judge the defects inside the concrete based on their amplitude, tough time, and frequency after passing through the concrete. Nevertheless, this technique has to know the position of the source locations[19]-[22].

1.2.6 Acoustic emission testing technology

The first case of applying acoustic emission testing technology is General Dynamics of the United States successfully used acoustic emission technology for the hydrostatic test of the Polaris missile shell in 1964[23]. This technology entered Japan in the 1970s; at the same time, also developing in Europe. This technique evaluates the extent of interior damage using stress waves that are released from the material itself (sound sources include: cracks, dislocations, and internal structure). Acoustic emission testing is a dynamic non-destructive testing technique that assesses the number of structural states and continuously monitors the status of the materials; and is frequently used to find faults with intricate forms with low environmental requirements. The significant advantage of this method could finish other non-destructive testing methods that cannot be used for testing flights might be completed using acoustic emission testing technologies (including high temperature, nuclear radiation, and highly toxic environments). Acoustic emission technology is used in niche industries, including steel corrosion, material degradation, and concrete fracture[24]-[25]. However, this technique could not be accurately detected if the material cannot release enough stress waves.

1.2.7 Acoustic Emission Tomography (AE tomography)

Schubert presented AE Tomography by merging elastic wave tomography and source localization technologies in 2004 based on elastic waves propagating straightly theoretically[26]. From 2012 through 2016, Kobayashi devised and used AE tomography in actual structures for two- and three-dimensional numerical simulation and experiments[27]-[28]. In addition, this technique is applied to concrete plates and RC bridge decks for bullet

trains. According to the fundamental principle of AE tomography, AE events are launched from an unidentified source location, and the receivers at the corresponding place correspondingly receive the elastic wave. Then, reconstructed the velocity distribution in the image stage that depends on each meshed cell's travel time is calculated based on the grid that has been separated in advance after measuring and collecting the arrival time. The most significant advantage of AE tomography is describing the structure inside of health conditions without the source location information. Compared with other non-destructive testing techniques, AE tomography could estimate the source locations of AE events and carry out elastic wave velocity distribution to evaluate the structures and has the advantage of using only one side of the structure to evaluate the healthy internal condition[29]-[32]. Each characteristic of non-destructive testing technology is shown in table 1.1.

Table 1.1. Characteristics of NDT technique.

NDT method	Characteristics
Infrared testing technology	Only possible in a laboratory setting
Radar wave testing technology	Electromagnetic waves will be shielded by steel in the RC
Impact echo testing technology	Could not test inside of the concrete
Ultrasonic rebound testing technology	Easily be affected by external factors
Ultrasonic testing technology	Source locations are necessary
Acoustic emission testing technology	Relay on the stress wave released from the material itself
Acoustic Emission (AE) tomography	**1) Could estimate the source locations** **2) Could use only one side of the structure to evaluate** **3) Various generating elastic waves can be usable**

1.3 Development of AE tomography

Schubert proposed AE tomography in 2004 by combining elastic wave tomography and source localization technology[36]. Theoretically, the propagation path of elastic waves in the medium is assured as a straight line.

In 2012, Yoshikazu Kobayashi developed Three-dimensional seismic tomography with tetrahedra element on isoparametric mapping method for concrete structure based on ray-trace and identification technique and simultaneously iterative reconstruction technique (SIRT) which is the statistical identification technique[37].

In 2014, Yoshikazu Kobayashi, Tomoki Shiotani, and Kenichi Oda introduced the algorithm of the three-dimensional AE-tomography on the basis of extended Kalman filter, which as

the reconstruction technique to control the weight of observation on velocity distributions and validated by the numerical investigation[38].

In 2015, Tomoki Shiotani, Satoshi Osawa, and Shohei Momoki executed AE monitoring and elastic wave tomography and did an experiment to visualize damage in RC bridge deck for bullet trains with AE tomography, verified AE tomography could provide AE source location and velocity distribution[31].

In 2016, Yoshikazu Kobayashi and Tomoki Shiotani introduced the computerized AE tomography, a novel procedure of advanced computerized tomography for elastic velocity measurement. The capability of this method was studied by numerical investigation and verified the application in existing planar structures and cylindrical specimens by laboratory experiments[29].

In 2016, Yoshikazu Kobayashi and Tomoki Shiotani studied two-dimensional Q-value AE-tomography and verification on numerical investigations, which only used observed AE data at receivers, and Q-value distributions on the basis of the method to visualize the distribution of the deterioration[39].

In 2017, Tomoki Shiotani, Takahiro Nishida, Hiroshi Nakayama and Yoshikazu Kobayashi etc. compared the elastic velocity distribution with elastic wave tomography and AE tomography based on RC bridge deck in wheel loading test to evaluate the fatigue failure of concrete bridge decks[40].

In 2019, Yiming Feng, Tomoki Shiotani, and Yoshikazu Kobayashi evaluated the damage in RC bridge decks reinforced with steel plates by AE tomography. The result shows that RC bridge decks with steel plates could be evaluated for existing or emerging defects using the tomographic method and AE measurement[30].

In 2019, Tomoki Shiotani, Takahiro Nishida, and Yoshikazu Kobayashi etc. devised an advanced measuring technique employing a tomographic methodology known as AE tomography without artificial excitations, which allowed for one-side access evaluation of massive infrastructures and was subsequently clarified by steel plate-bonded RC slabs experimental test[32].

1.4 Innovation point of this study

In the initial research, compressive sampling theory was applied to the elastic velocity distribution in the imaging stage of the elastic wave velocity distribution. It is overcoming the traditional algorithm demand for a large amount of measurement data and proving that a small measurement path can be used to obtain the same level of accuracy in the result.

This study aims to improve the quality of the velocity distribution in the image stage of AE tomography. Given the characteristics of AE tomography, this study applies the LASSO algorithm to the velocity distribution reconstruction stage of AE tomography. The research carried out 2D numerical simulation and 3D numerical of concrete failure types from reality. Furthermore, the feature and corrections of the proposed method were verified by experiments. This study explores the practicability and evaluation ability of the LASSO algorithm to work on AE tomography.

1.5 Outline of the thesis

Chapter 1 briefly introduces the research background, the classification of standard non-destructive testing techniques, the advantages and disadvantages of each technique, the characteristics and advantages of AE tomography, the research process of AE tomography, and the purpose of this research and innovations.

Chapter 2 introduces the basic theory and methodology of AE tomography, the calculation process, and the theoretical combination of the proposed method LASSO with AE tomography.

Chapter 3 introduces the verification of elastic wave velocity tomography based on compressive sampling, which is verified by numerical simulation. This part explains the basic theory of compressive sampling, the theory combined with elastic wave tomography, and the calculation process. Furthermore, the numerical simulation results of compressive sampling were compared with the traditional SIRT algorithm to verify the proposed method.

Chapter 4 studies the range of lambda parameters through numerical simulation while LASSO theory is applied in AE tomography and investigates the detection ability of the proposed method via numerical simulation. Furthermore, three typical concrete defeat types are analyzed by numerical simulation and verified by the results of the traditional SIRT algorithm. The methodology and numerical simulation of 3D AE tomography are elaborated on in the final part.

Chapter 5 introduces three experiments calculated by the proposed LASSO algorithm. The first one is the experiment on an aluminum plate with artificially defective to validate the proposed algorithm work or not and compare the velocity distribution result with the traditional algorithm SIRT to verify the advantage of the LASSO algorithm. Secondly, the experiment specimen is a concrete slab with a small narrow defect area embedded in the middle of the concrete. Finally, the non-destructive testing of the concrete prefabricated retaining plate is carried out using the proposed theory, and the results of SIRT are compared to verify the effectiveness of the algorithm.

Chapter 6 summarizes the work conducted and perspectives for future research on this subject and drawn.

2 THEORY OF AE TOMOGRAPHY AND PROPOSED METHOD

This chapter introduces the basic theory of AE tomography and the traditional algorithm of velocity reconstruction. Furthermore, the primary method of the LASSO algorithm combined with AE tomography was explained in the next part. According to the fundamental theory of AE tomography, AE events are emitted from an unknown transmitting location, and receivers at the appropriate place receive the elastic wave. After detecting and accumulating the arrival time, the travel time of each mesh cell is computed based on the previously-divided grid. Lastly, the findings evaluate the defect's size and area based on the velocity distribution applied by the reconstructing procedure. The existing mainstream inversion algorithms, such as SIRT, acquire the velocity distribution and visualize the internal damage of structure, which is conventional and mature to apply in practice[41]. In order to generate the velocity distribution, the conventional technique necessitates an insufficient quantity of event data, which is a critical flaw. SIRT, for instance, uses a specific amount of event data to derive the velocity distribution by repeatedly iterating over each cell. Meanwhile, the faulty region's features are localized relative to the extent of the structures, and it meets the requirements for using the Lasso regression to generate an accurate velocity distribution while needing a smaller quantity of event data.

2.1 Basic theory of AE tomography

AE tomography is a non-destructive testing method that uses the arrival time of elastic waves to identify the AE source locations and velocity distribution. The source locations and velocity distribution are analyzed concurrently and influence each other during the analysis. The AE source locations are computed based on the assumed elastic wave velocity distribution from the relay point to the receiver, and the velocity is reconstructed using the travel time between the AE sources and the receivers based on the estimated elastic wave velocity distribution. The arrival time is derived from the emission time and first travel time. The velocity is then updated by revising the location of AE sources depending on the mesh cells. The position of the AE source is considered to be the location of the homogenous velocity of the material in each mesh cell, as determined by the starting velocity distribution. After determining the emission time, the tomography approach will be implemented[32]. The AE tomography flowchart is displayed in Figure 2.1. It is noted that this process uses the straight-line ray path based on the homogeneity of the elastic wave velocity distribution. The travel time spanning from the nodal point to the receiver ΔT_{ik} is determined by the following hypotheses:

$$\Delta T_{ik} = \sum_{j=1}^{n} S_j \, l_j \qquad (2.1)$$

in which n is the number of the meshed elements, j is the number of elements, i represents the ith receiver, k depicts the kth nodal and relay point to be accessed, slowness is the reciprocal of elastic wave velocity represented as S_j and l_j is the ray-path length in cell j.
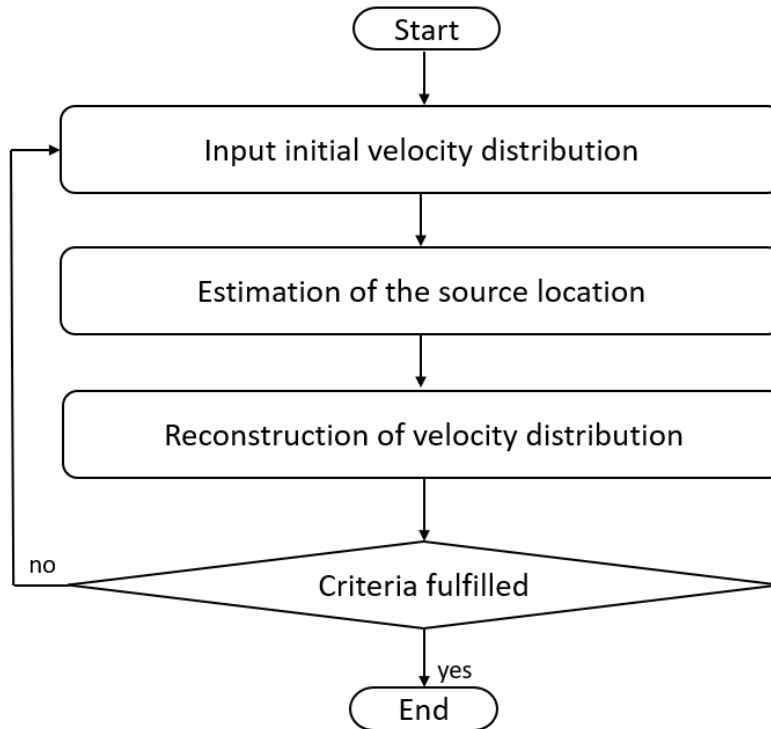

Figure 2.1 Flowchart of AE tomography.

In the first stage, the source location and emission time of AE events are calculated by using the arrival times according to the initial elastic wave velocity distribution and the receiver's position. In order to acquire the theoretical travel time, the second stage is to calculate the sum of the estimated emission time and the travel time from the estimated source location to the receiver[33]. Finally, the velocity distribution is reconstructed and updated by minimizing the difference between the theoretical and measured travel times. These two stages are performed iteratively until the convergence criteria are satisfied and the source position and the elastic wave velocity are determined simultaneously. In the following subsections, the procedure of each stage is briefly introduced.
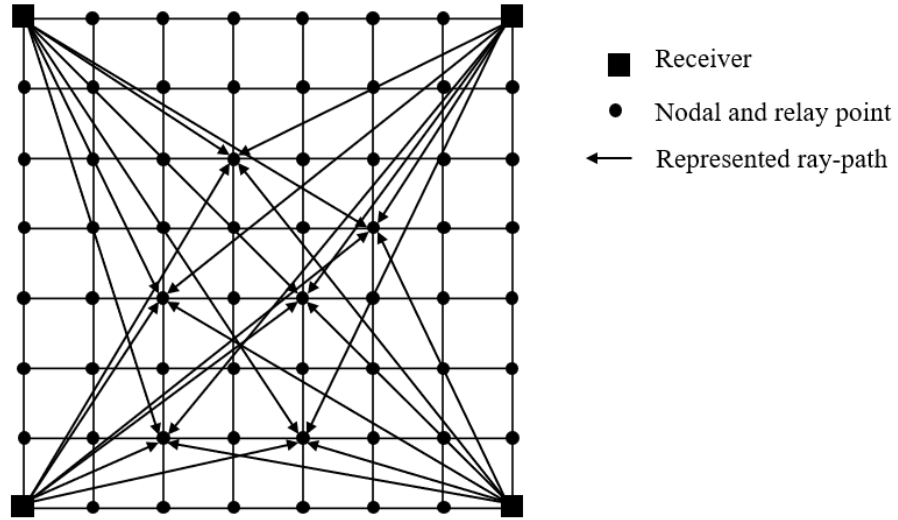
Figure 2.2 Potential emission time computation.

The source location is estimated from velocity distribution, the location of the receiver, and the arrival times of the AE in AE tomography[29]. The source location estimation starts with calculating the potential emission time. The idea of the computation of the potential emission time is shown in Figure 2.2. The potential emission time is calculated from the results of the ray trace between the receiver to each nodal and relay point as follows:

$$P'_{ik} = A_i - \Delta T_{ik} \tag{2.2}$$

where i represents the ith receiver, k depicts the kth nodal and relay point to be accessed, A_i is the observed arrival time at receiver i. P'_{ik} is the potential emission time at point k. The potential emission time denotes the time at which an AE event is expected to be emitted at the point k if the observed arrival time at the receiver i is A_i on the present elastic-wave velocity structure. This study is carried out for every receiver connected with a single measurement event. Assuming n receivers are placed, each node has n possible emission timings for a single event. When the elastic wave velocity distribution and ray path are exact, the potential emission time should be able to follow the proper source location. Due to inadequate velocity dispersion in this source location procedure, it is often chosen based on the nodal and relay point with the smallest possible emission time variation. By expanding node and relay locations, AE Tomography could improve the precision of source location and emission time. Figure 2.2 details the relay points inside each cell. At each division point, an orthogonal straight line is drawn to the edge. Relay points are created at the intersections of straight lines and edges. Since relay point density and calculation cost are related, it is vital to identify the optimum density of relay points prior to computation. The average of the potential emission time O'_k at the source location is shown as:

$$O'_k = \frac{1}{n}\sum_{i=1}^{n} P'_{ik} \tag{2.3}$$

This value is utilized in the reconstruction algorithm described in the subsequent section. The velocity distribution is determined by comparing the observed and theoretical travel times. Typically, the source location is established based on the mean potential emission time at the nodal or relay point with the minimum variance. The theoretical arrival time A'_i of receiver i showed as follows:

$$A'_i = O'_k + \Delta T_{ik} \tag{2.4}$$

It is noted that ΔT_{ik} is the travel time from the receiver to the nodal and relay point selected as the source location correspondingly. In AE tomography, the traditional method of SIRT iteratively processes comparison measurement data to construct the velocity distribution representation of an internal physical structure. The SIRT algorithm equation is as follows:

$$S_j^{(I)} = S_j^{(I-1)} + \Delta S_j \tag{2.5}$$

$$\Delta T_i^{(I-1)} = T_{oi} - \Delta T_i^{(I-1)} \tag{2.6}$$

$$\Delta t_{ij} = \Delta T_i^{(I-1)} \cdot l_{ij}/L_i \tag{2.7}$$

$$\Delta S_j = \sum_i \Delta t_{ij}/\sum_i l_{ij} \tag{2.8}$$

Where I is the iteration times and j is the cell number, i is the number of ray. $S_j^{(I)}$ means slowness of cell j in iteration I, T_{oi} is observed travel time, $\Delta T_i^{(I-1)}$ is the theoretical travel time of ray i for the $(I$ -$1)$th iteration. l_{ij} is the ray length of i in j cell, and L_i is the ray length between the source location to receiver[34]. Obviously, the SIRT method requires a large amount of event data for iterative computation. However, these techniques have their own limitations, such as requiring sufficient event data for velocity reconstructions. This study used Lasso regression for AE tomography to overcome these shortcomings.

2.2 LASSO algorithm combines with AE tomography

In 1995, Tibshirani proposed Lasso (least absolute shrinkage and selection operator), a regression model that uses L1 regularization techniques, also referred to as Lasso regression. Regularization is a general term for a class of methods that introduces additional

information to the original loss function in order to prevent overfitting and improve model generalization performance. There are generally two commonly used extra items called L1 regularization (ℓ1−norm) and L2 regularization (ℓ2−norm). L1 regularization and L2 regularization can be regarded as penalty terms of the loss function, and penalty refers to some restrictions on some parameters in the loss function[35]. The algorithm also performs on solving convex-cardinality problems as an essential reconstruction algorithm (also called the L1 heuristic) rebuilt from the L1-norm[41]-[43]. It is an efficient approach to reconstructing sparest solutions to specific underdetermined systems of linear equations. More specifically, there is an unknown vector $x \in R^N$ and an underdetermined matrix $A \in R^{M \times N}$ and y = A · x. The problem can be solved as follows:

$$\min \|x\|_1 \text{ subject to } \|A \cdot x - y\|_2 < \varepsilon \tag{2.9}$$

Where,$\|\cdot\|_1$ and $\|\cdot\|_2$ represent the L1-norm and L2-norm, respectively, and ε represents the noise boundary[44]. According to this algorithm's characteristic, LASSO regularization could make parameters sparse, and the resulting sparse matrix can be used for feature selection. The feature of this theory might help reduce the number of matrix coefficients while concurrently providing local optimum solutions. In other words, the LASSO technique needs fewer measurement paths than other algorithms, such as SIRT, for velocity distribution in elastic velocity tomography, where the number of coefficients depends on the number of paths. The following demonstrates the theory of AE tomography combined with LASSO algorithm:

$$T = A \cdot (s_0 + \Delta s) \tag{2.10}$$

T is the vector of measurement travel time, S_0 is the standard slowness in a completely healthy state, and Δs is the slowness difference vector generated by subtracting the actual slowness from the standard slowness. All of the ray-path matrices are used to construct A, a coefficient matrix that is generated from all of the travel lengths. If T_0 is the travel time vector for a healthy specimen and is defined as

$$y = (T - T_0) = A \cdot \Delta s \tag{2.11}$$
$$\text{,where } T_0 = A \cdot s_0$$

Where y is a vector representing the results of the deviation between the measured travel time and the travel time in totally healthy conditions. The velocity distribution imaging of AE tomography depends on reconstructed Δs in equation 2.12, which is defined by the LASSO algorithm after the sampling phase from equation 2.9. It is noted that soluting the slowness vector Δs is a defect detection problem in physical understanding.

$$\min \|\Delta s\|_1 \quad \text{subject to} \quad \|A\cdot\Delta s-y\|_2 < \varepsilon \qquad\qquad (2.12)$$

The $\|\cdot\|_1$ and $\|\cdot\|_2$ are the L1-norm and L2-norm, respectively. While it would be more forceful to adopt λ, which is the Lagrangian multiplier (regularization value parameter) in identifying the velocity distribution stage, to provide a balance between ($\|A\cdot\Delta s-y\|_2$) and the constraint($\|\Delta s\|_1$) for data misfit[45]-[46]. Equation 2.12 will update to equation 2.13：

$$\operatorname{argmin} (\|A\cdot\Delta s-y\|_2 + \lambda\|\Delta s\|_1) \qquad\qquad (2.13)$$

It is noticed that the slowness distribution is updating during the iterative procedure. In accordance with Figure 2.1, it is necessary to evaluate whether the criterion is fulfilled or not after a process of calculation, the source location, and updating the slowness distribution are iteratively conducted.

3 VERIFICATION OF ELASTIC WAVE VELOCITY TOMOGRAPHY BASED ON COMPRESSIVE SAMPLING

This chapter validates the compressive sampling (CS) based elastic wave velocity tomography (EWT) method. Traditional elastic wave velocity tomography requires considerable time and labor. Nonetheless, given the primary assumption of the CS algorithm is to reconstruct the original velocity distribution from a subsample of random measurements, compressive sampling is used to overcome this difficulty. During the measurement step, the CS algorithm picked fewer paths among all measurements. In the visualization phase, the L1-minimization optimization approach is then used to recover the damaged area and magnitude. The CS method is superior to the traditional elastic wave velocity tomography algorithms because it dramatically decreases the measuring burden and achieves a high degree of reconstruction precision.

3.1 Overview

Under the premise of causing damage to the structures, the transmitter emits an elastic wave, which is received by sensors in order to determine the interior status of the structures. In elastic wave tomography, elastic waves are generated by events, which are then collected by positioned receivers. On the basis of the predetermined grid division, the travel time of each event is computed to produce the velocity field distribution in order to estimate the amount and location of the damage.

After the measurement phase, established inversion techniques such as SIRT and ART are commonly utilized. Visualize the interior damage of the concrete as a velocity distribution during this time. If the amount of measurement data is insufficient, these methods have difficulty obtaining the velocity distribution appropriately. Generally, a huge quantity of measuring data is required, which accrues substantial expenses. Due to the rarity of concrete damage, CS theory could overcome these difficulties while achieving correct findings needs only a small amount of measuring labor.

The second section of this chapter presents the fundamental theory of compressive sampling, the theoretical calculation procedure, and the criteria. The third section discusses the theory of compressive sampling paired with elastic wave tomography and establishes the algorithm's viability by determining the pertinent parameters. In the fourth section, numerical simulation results are presented and compared with SIRT results to demonstrate the capacity of the CS algorithm.

3.2 Compressive sampling algorithm

In 2006, E. Candes, D. Donoho, and T. Tao proposed the innovative theory of compressive sampling[47]-[50]. CS theory recommends acquiring data in a compressed format for massive data collection and compression, in contrast to acquiring the complete data and then compressing it. According to the traditional Nyquist sampling principle, the sampling frequency must be more than twice the sampling's maximum frequency in order to preserve the signal's original integrity. Due to the relatively high signal frequency, a tremendous amount of sampling data is needed under the conventional idea. However, from a different viewpoint of compressed sensing, the sparseness of the signal must be considered rather than the sampling frequency, and the original signal may be reconstructed if the signal form is sufficiently sparse[51]. Figure 3.1 displays the fundamental flowchart:
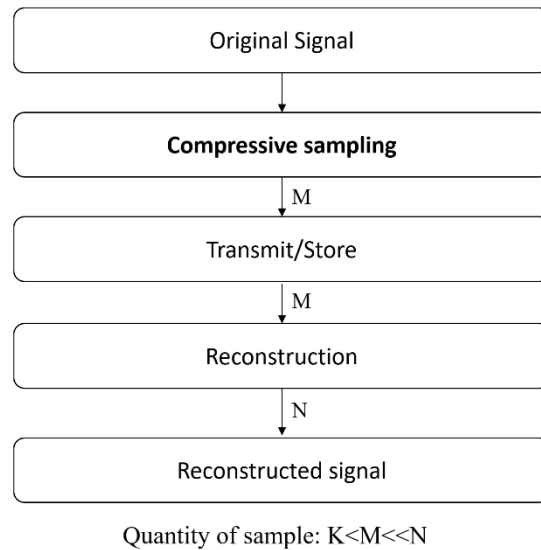
Figure 3.1 Flow chart of CS theory.

The primary property of compressive sampling is that the signal may be retrieved from far fewer measurement samples than from traditional methods. Typically, the constituents of a one-dimensional signal x, which may be seen as an $n \times 1$ column vector in R^N, are x [n], where n = 1,2,..., n. The signal in its high-dimensional form may be simultaneously vectorized into a lengthy one-dimensional vector. The signal x could be generated sparser to use the $n \times n$ basis matrix ψ and shown in equation 3.1. It is essential that the signal x be more compressible if it is sufficiently sparse.

$$x = \Psi\alpha \qquad\qquad (3.1)$$

Where $\alpha \in R^N$ is a vector of k non-zero elements (k <<n, k-sparse), $\psi \in R^{N \times N}$ is the basis matrix, Φ is measurement matrix as a random matrix (normally is Gaussian matrix and Bernoulli matrix), and y could be described as:

$$y = \Phi\psi\alpha + n = \Theta\alpha + n \qquad (3.2)$$

The dimension of the transfer matrix Θ is m × N, and the number of rows of the matrix Θ is much smaller than the number of columns of Θ. Ψ is the sparse matrix. Noise should be taken into consideration during the measurement process and represented as n in the formula. Generally, it is an ill-posed problem to recover α from the measured value y. Convex optimization algorithms can solve this mathematical problem. There is a condition named restricted isometry property (RIP) related to the signal x, and the transition matrix Θ must satisfy in order to use this theory[52], shown as follow:

$$1-\delta \leq \frac{\|\Theta v\|_2}{\|v\|_2} \leq 1+\delta, \delta > 0 \qquad (3.3)$$

Restricted isometry property (RIP) means that for k belonging to any integer, there is an isometric constant δ that satisfies the above relationship. In addition, $v \in R^N$ is all K-spare vector and δ is the minimum value that satisfies the vector v with any sparsity. Both conditions of each column of the matrix Φ must be orthogonal, and cardinality is more minor than k should be satisfied. The following equation could decide the measurement quantity:

$$m > \mu \cdot K \cdot \log(N/K) \qquad (3.4)$$

Where, μ is a constant with a stationary value, in this study $\mu = 4$. Assuming that all the above requirements are sufficient, the vector x can be accurately reconstructed from the vector y. Then, the following equation of the convex optimization algorithm is applied to solve this ill-posed problem.

$$\min \|\alpha\|_1 \text{ subject to } \|\Theta\alpha - y\|_2 < \varepsilon \qquad (3.5)$$

Where, $\|\cdot\|_1$ is the L1-norm and $\|\cdot\|_2$ is the L2-norm, ε is the noise bound.

3.3 Implementation of CS algorithm in elastic wave velocity tomography

3.3.1 EWT theoretical elaboration

In the field of civil engineering, elastic wave tomography is utilized to discover and diagnose internal damage to the structure and aged concrete components, such as piers and walls [53]. The underlying idea is that the inhomogeneity of the medium affects the velocity of propagation of elastic waves, which implies that the propagation velocity in undamaged concrete remains constant. However, the velocity of propagation reduces when elastic waves contact holes or fractures in structures. Thus, the velocity distribution graph is shown in order to assess the state of the concrete's inside. The travel time along a measuring path could appear as follows:

$$T_i = \int_{L_i} \frac{1}{V(x,y)} dL = \int_{L_i} s(x,y) \, dL \tag{3.6}$$

T_i is the travel time in i^{th} path, and L_i is the ith measurement path length from the source to sensor, $V(x, y)$ is velocity function, and $s(x, y)$ is slowness. The reciprocal of the velocity is titled slowness[54]. In order to locate the defect degree and position in the specimen more precisely, the whole inspection area is divided into subdivision units. The sum of the travel time of each subdivision unit can be expressed as follow:

$$T_i = \sum_{j=1}^{w} \frac{a_{ij}}{V_j} = \sum_{j=1}^{w} a_{ij} \, s_j \tag{3.7}$$

where a_{ij} is the travel length of jth grid in i^{th} path, V_j is the velocity of jth, and S_j is the slowness of the jth. The description above is the travel time of each path, and the following formula can be expressed for all the measurement paths.

$$T = A \cdot \frac{1}{V} = A \cdot s = A \cdot (s_0 + \Delta s) \tag{3.8}$$

Where T is the vector of the travel time, and A is the travel length matrix, V is velocity, S is the vector of the slowness, S_0 is the vector of the standard slowness, and Δs is the vector of the difference of the slowness.

The equation defining the internal velocity of concrete could be determined by the following computations. Traditional algorithms (such as ART, SIRT, etc.) iterate through relative measurement data to generate a velocity distribution image of an interior concrete structure. However, these algorithms have their own restrictions, for instance, need a high ratio of measurement routes, a great deal of data, and enormous labor expenses. This research used a technique called compressive sampling for elastic wave tomography, which may address these deficiencies and is acceptable for elastic wave tomography. It is possible to do computations with the same degree of calculation precision.

3.3.2 CS applying in EWT

If the damage to a concrete structure is minimal, merely a few localized areas are affected, while the majority of the structure remains intact. In elastic wave tomography, the CS algorithm could utilize this fundamental concept. In typical concrete constructions, the propagation speed of elastic waves is around 4000 meters per second. Consequently, the condition of the interior concrete damage could well be determined by measuring the rate of decay in each section of the concrete buildings. The following demonstrates the theory of elastic wave tomography paired with compressive sampling:

$$T = A \cdot (s_0 + \Delta s) \tag{3.9}$$

Where, T is the measurement travel time vector, and S_0 is the standard slowness in totally healthy conditions, Δs is the slowness difference vector that is obtained as the difference between actual slowness and standard slowness. A is a coefficient matrix of the travel lengths that is generated from all of the ray-path matrices. If T_0 is the travel time vector if the specimen is healthy, and T_0 is described as

$$T_0 = A * s_0 \tag{3.10}$$

Where y is the random sampling results of the difference between the measured travel time and the standard travel time. Φ is the measurement matrix that obeys random Bernoulli distribution and contains only one "1" emerging in each row and column. 1 means that the travel time data are selected, and 0 means these data are omitted in the measurement stage. Φ is shown as follows:

$$\Phi = \begin{bmatrix} 1 & 0 & 0 & \cdots & 0 \\ 0 & 0 & 1 & \cdots & 0 \\ 0 & 1 & 0 & \cdots & 0 \\ \vdots & \vdots & \vdots & \ddots & \vdots \\ 0 & 0 & 0 & \cdots & 1 \end{bmatrix}_{m \times N} \tag{3.11}$$

After the sampling stage, the elastic wave tomography image is reconstructed using equation 3.12, which employs the L1- minimization algorithm[54].

$$\Delta \hat{s} = \text{argmin} \left(\|\Theta \Delta s - y\|_2 + \lambda \|\Delta s\|_1 \right), \text{ where } \Theta = \Phi \cdot A \tag{3.12}$$

With $\Delta \hat{s}$ is a vector that shows the difference between the slowness from the standard slowness and λ is the regularization parameter, which is 0.083 in this study. $\|\cdot\|_1$ and $\|\cdot\|_2$ are L1-norm and L2-norm correspondingly[45]. Both the RIP and incoherence criteria are satisfied by the transfer matrix $\Theta = \Phi \cdot A$.

$$y = \Phi \cdot (T - T_0) = \Phi \cdot A \cdot \Delta s \tag{3.13}$$

3.4 Numerical simulation results and analysis

3.4.1 Model and conditions for the numerical analysis

In a series of numerical studies, the results of the CS algorithm and the SIRT method are compared in order to validate the CS algorithm for elastic wave velocity tomography. In addition to correcting the slowness factor from ray lengths and travel time residuals in a chosen cell[55], the SIRT algorithm proportionally distributes travel time residuals in each pathed cell and corrects the slowness factor from ray lengths and travel time residuals in the selected cell.

The following are the fundamental characteristics of the numerical simulation model: The dimensions of the concrete slab model are 10 m × 10 m, there are 100 random occurrences, and there are 20 receivers. Figure 3.2 depicts the dispersion of initial velocity. The blue section represents healthy concrete with a velocity of 4000 m/s, whereas the red section represents damaged concrete with a velocity of 3000 m/s. The twenty receivers are put on the model's edges with a two-cell spacing between each, as shown in figure 3.2 mesh information and receiver locations. Using 2000 samples from the preceding section, matrix Φ randomly selects 50 measurement pathways. In this investigation, the number of pathways selected meets the requirement $m>u·K·log(N/K)$. Therefore, the transfer matrix Θ = Φ * A has dimensions of 50 × 100. The reconstructed image is restored using the L1 minimization procedure.
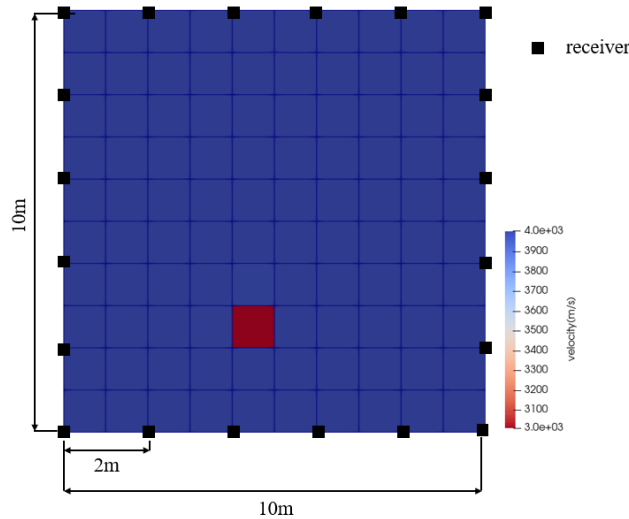
Figure 3.2 Original velocity distribution.

3.4.2 Results and discussion

Figures 3.3 (a) and 3.3 (b) illustrate the velocity distribution of reconstructed elastic waves based on CS and SIRT, respectively. The reconstructed results indicate that the red area with a lower velocity distribution is the damaged area, while the navy blue area with a higher

velocity distribution is a healthy condition. In compared to the SIRT method, the CS algorithm has 50 measurement routes as contrasted to 2000. It is remarkable that these two algorithms were able to recover the target's damage so precisely despite having vastly differing amounts of measurement data.

(a) Result of CS Algorithm.   (b) Result of SIRT Algorithm.
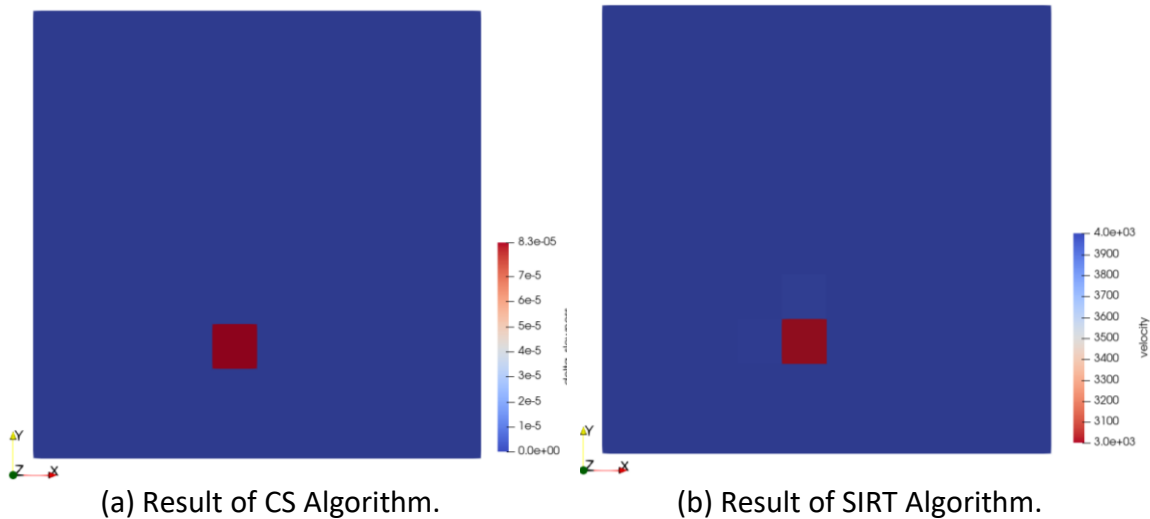
Figure 3.3 Reconstructed velocity distribution.

3.5 Conclusion

This study verified elastic wave velocity tomography based on compressive sampling algorithm. Through the series of numerical investigations, the effectiveness of the CS algorithm applied to elastic wave tomography was confirmed. Considering the sparseness of concrete failure under normal circumstances, this is the prerequisite for utilizing CS theory. After randomly sampling the elastic wave testing in the measurement stage and restoring the reconstructed calculation, accurate results comparable with SIRT are obtained. The CS algorithm requires fewer measurement paths than the classic SIRT algorithm, which dramatically reduces the amount of calculation while maintaining the same accuracy. The calculation results show that this method can accurately locate the position of concrete injury and detect the degree of damage with extraordinary efficiency.

4 NUMERICAL SIMULATION OF AE TOMOGRAPHY

Based on the previous methods, this chapter conducts severe research by numerical simulations in AE tomography. Firstly, it is crucial to study the lambda parameters in LASSO suitable for AE tomography. Then the simulation models of different damage types and percentages of damage area occupied proportion are studied to detect the ability of the proposed method. Lastly, the different types of numerical simulations are compared with SIRT according to the actual concrete failure type to verify the LASSO algorithm.

4.1 The study for lambda in LASSO algorithm

In this section, numerical simulations are performed for different lambda values to determine the lambda range suitable for AE tomography. It is noted that the reconstructed velocity distribution uses formula 2.13 from chapter 2. In LASSO, the value of lambda affects the resulting quality of the velocity distribution of non-destructive testing. If the lambda is not in the correct range, the correct velocity distribution cannot be obtained. As a result, the damaged area cannot be effectively detected, the detection area will be misjudged, and the detection quality will be affected. In order to study the lambda, eleven different lambda values, 0.01, 0.02, 0.04, 0.06, 0.08, 0.083, 0.09, 0.2, 0.4, 0.8, 1, were selected for numerical simulation calculations. The model overview is shown in the following table:

Table 4.1 Model information.

Size of model	1 m × 1 m
Size of damage area size	0.1 m × 0.1 m
Initial velocity	4000 m/s
Number of sensors	20
Number of mesh	100
Number of events	100
Number of relay points for each cell	12
Number of measurement paths	1000

Numerical models are used to identify the fault locations and demonstrate the implementation in order to study the rational value range of the LASSO method on the AE tomography. The initial velocity distribution is shown in figure 4.1. The red region shows the defective status with a velocity of 3000 m/s, while the blue area indicates concrete in excellent condition with a velocity of 4000 m/s. The size of the model is 1 m × 1 m, and the value of lambda λ chosen as 0.01, 0.02, 0.04, 0.06, 0.08, 0.083, 0.09, 0.2, 0.4, 0.8, 1, respectively, to study the appropriate range. The initial elastic wave velocity for AE tomography is supplied as a uniform distribution of 4000 m/s. There are twenty sensors spaced 0.2 meters apart, placed around the perimeter of the model. There are 100 meshes, and each mesh contains 12 relay points. The model has 100 source locations at random,

shown by the white dots in figure 4.1. Finally, there are 1000 measurement paths in the model.
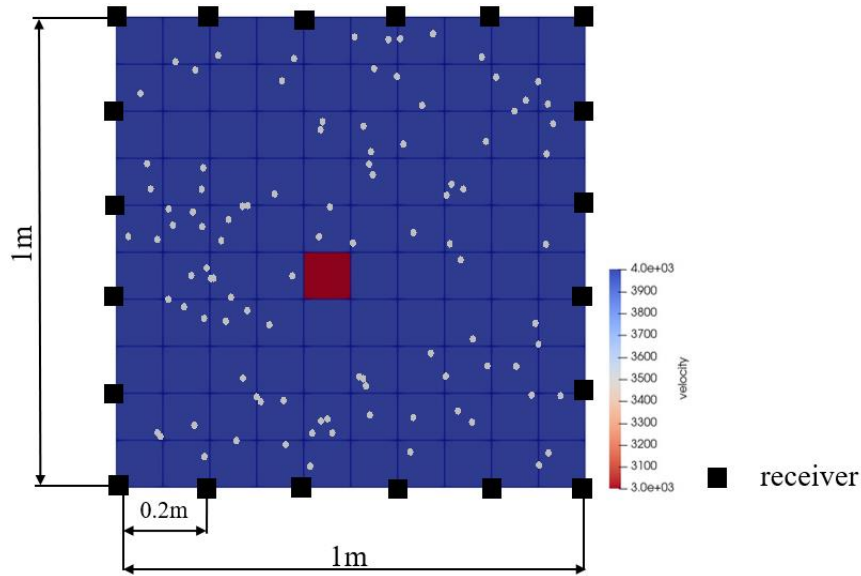
Figure 4.1 Initial velocity.

Following is the calculating procedure: 1) The arrival time at receivers could be determined utilizing the straight path from the generating source to every receiver. 2) The velocity distribution is reconstructed using the estimated arrival time with the LASSO algorithm in different values of lambda to investigate the suitable value range.

(a) Lambda is 0.01.

(b) Lambda is 0.02.

(c) Lambda is 0.04.

(d) Lambda is 0.06.

(e) Lambda is 0.08.

(f) Lambda is 0.083.

(g) Lambda is 0.09.
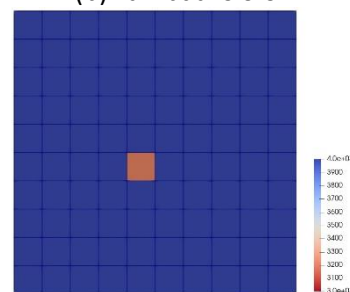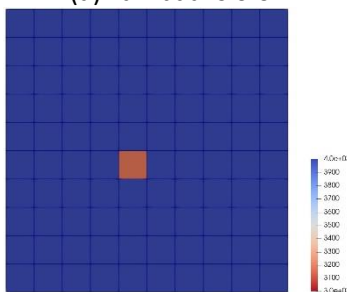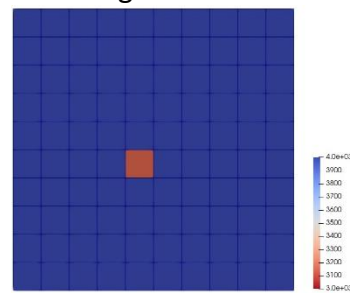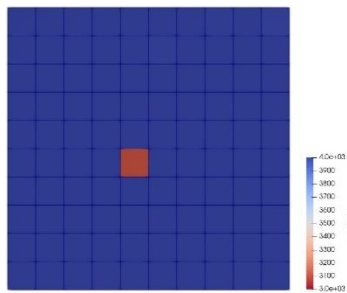
(h) Lambda is 0.2.

(i) Lambda is 0.4.

(j) Lambda is 0.8.
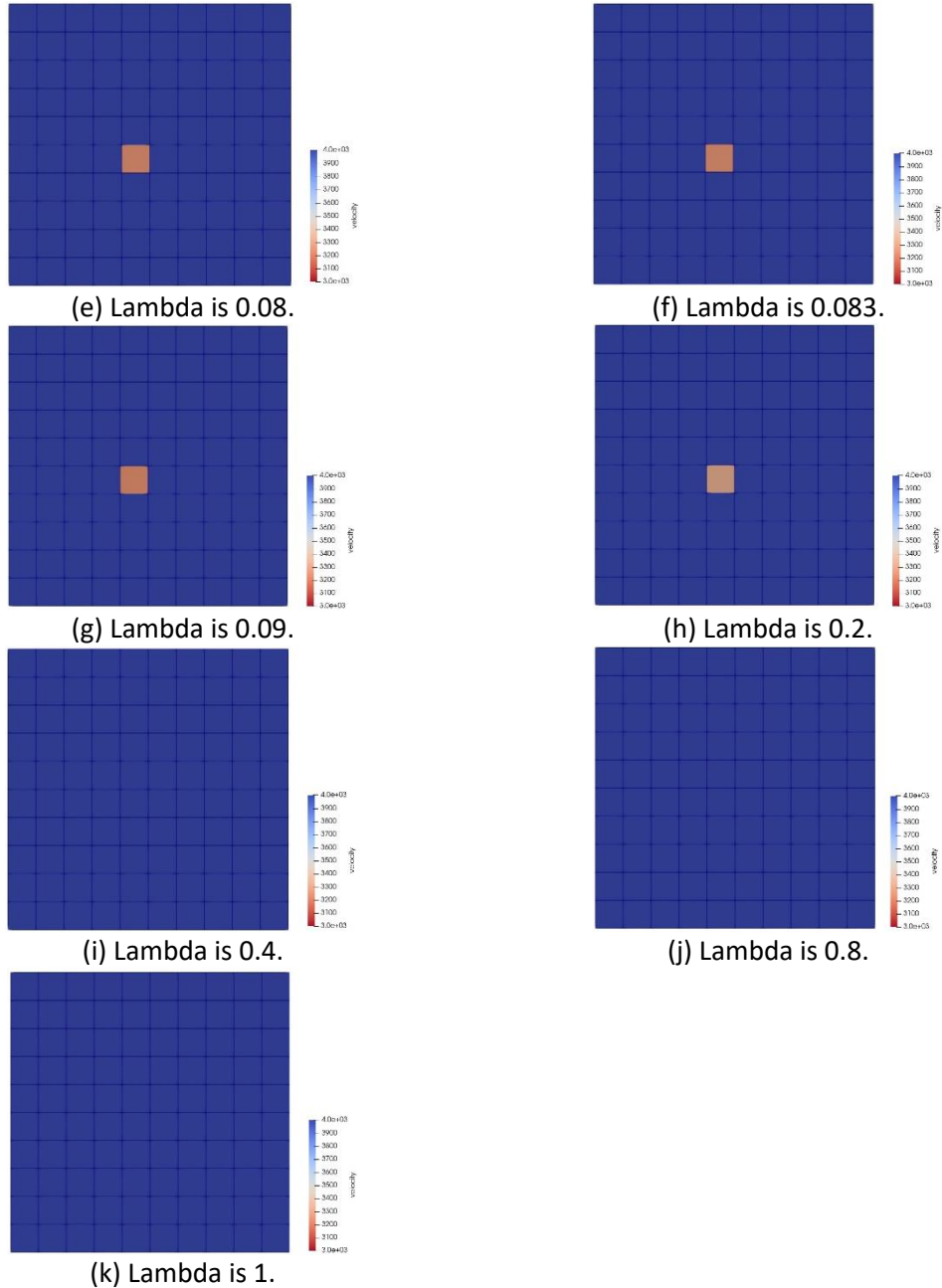
(k) Lambda is 1.

Figure 4.2 Calculated results.

According to the methodology in chapter two to describe the effect of lambda in the LASSO algorithm, the range becomes smaller if lambda is bigger, and vice versa. This section selects a relatively simple model with only one cell-destroying numerical simulation model to study the parameter lambda. The calculation results are shown in figure 4.2, the blue area is the high-velocity area indicating that the concrete is in healthy state. According to the velocity reconstruction results of 11 different lambda values

calculated respectively, it is noticed that the low-velocity area boundary and value can be clearly presented when the lambda is less than or equal to 0.2. The damaged area and low-velocity value cannot be identified when the lambda value is more extensive than 0.2, and the low-velocity area describes as a health condition that the algorithm is invalid. The healthy area in all of the models, which has a high-velocity area, is not entirely equal to 4000m/s when the lambda is small, which means that there is a very small shadow. It is not apparent in the above-reconstructed velocity results because the value is minimal.

Table 4.2 Error of L2-norm.

λ value	L2-norm error
0.01	115.2049
0.02	140.8557
0.04	172.8871
0.06	213.4071
0.08	269.0215
0.083	270.4199
0.09	258.888
0.2	344.8693
0.4	999.1048
0.8	999.9362
1	999.9848
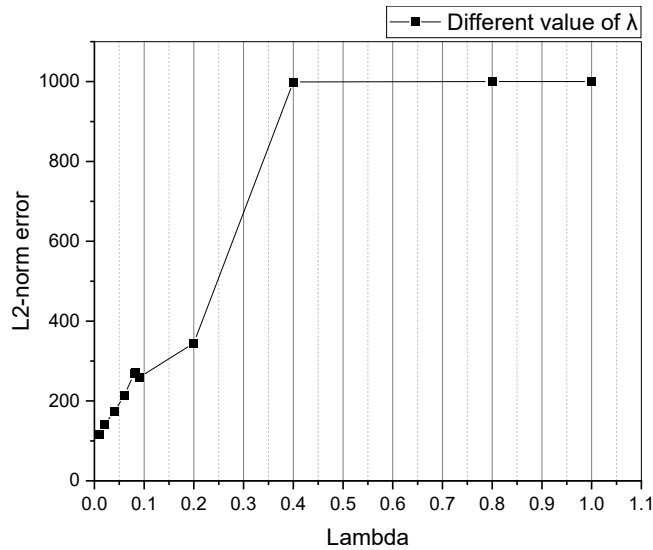
Figure 4.3 Error of L2-norm in different values of lambda.

The L2-norm errors of different lambdas are calculated as shown in figure 4.3 and table 4.2. According to the results, when the lambda is less than 0.2, the value of reconstructed velocity distribution by the LASSO algorithm is within a reasonable range. It is worth noting

that when the lambda is less than 0.9, the L2-norm error is small. When the lambda is more significant than 0.4, the L2-norm error suddenly increases and tends to be flat. It indicates that the error generated by the lambda is substantial and combined with the result of reconstructed velocity distribution, and it is not practical. It is noted that the study in this subsection is on the approximate scope of lambda for AE tomography because different computational models have different sizes, numbers of sensors, mesh thickness, relay points, number of events, and measurement paths. It means that the results have slight differences in reconstructed velocity distribution results.

According to the study in this subsection, it is suggested that the value of lambda suitable for AE tomography should be less than 0.2, preferably less than 0.09, and the specific value should be fine-tuned according to different models to obtain the expected velocity distribution.

4.2 Ability of LASSO algorithm

In order to study the capability and scope of application of the LASSO algorithm on AE tomography, numerical models are adopted to detect the fault areas and illustrate the implementation. There are six models (with two different types, one is concentrated and the other is strip in defected area) that have three different ratios of the defect area, as illustrated in figures 4.5 and 4.6.

The blue area indicates that the concrete in healthy condition has a velocity of 4000 m/s, and the red area denotes defective status with a velocity of 3000 m/s. The size of each model is 1 m × 1 m, and the damaged area occupies 10 %, 20 %, and 30 % of the two shapes of the model, respectively. The initial elastic wave velocity is 4000 m/s given as uniform distribution for AE tomography. The total number of sensors is twenty, which is set around the model's edge with an interval of 0.2 m. The number of mesh is a hundred, and each meshed cell has 12 relay points, as shown in figure 4.4. One hundred source locations are randomly generated in the model described as the white spheres in figures 4.5 and 4.6. The number of measurement paths for every model is 2000 in consequence.

● Relay point

○ Nodal point
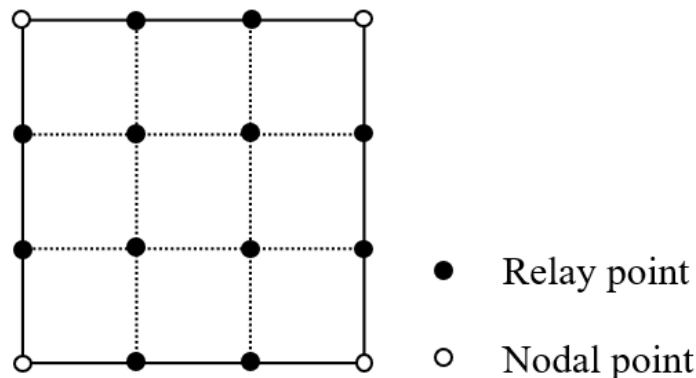
Figure 4.4. The setting of the relay point for each cell.

The calculation step will be as follows: 1) The straight path from the generating source to each individual receiver could be utilized to calculate the arrival time to the receivers. 2) the velocity distribution is reconstructed by using the computed arrival time with SIRT and LASSO to compare the target and resultant velocity distribution to investigate the capability of the proposed method.

| (a) Damage area 10 cells (10 %). | (b) Damage area 20 cells (20 %). | (c) Damage area 30 cells (30 %). |
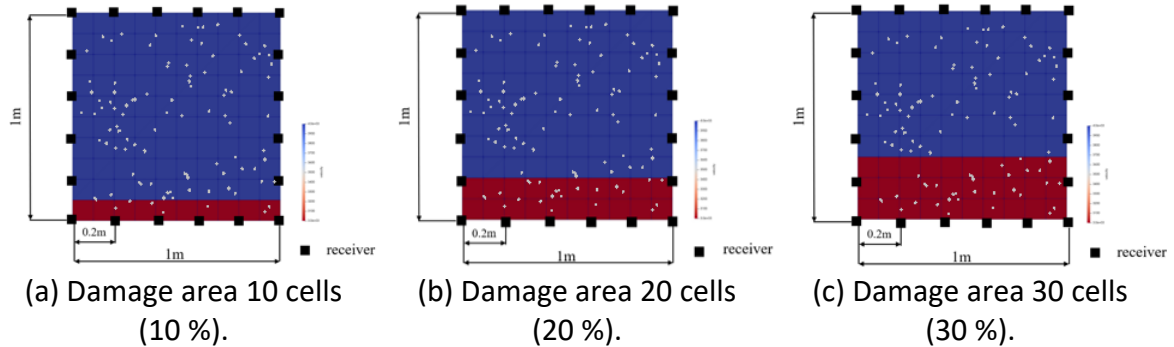
Figure 4.5 Strip types of damaged area with different rates of original distribution.

| (a) Damage area 10 cells (10 %). | (b) Damage area 20 cells (20 %). | (c) Damage area 30 cells (30 %). |
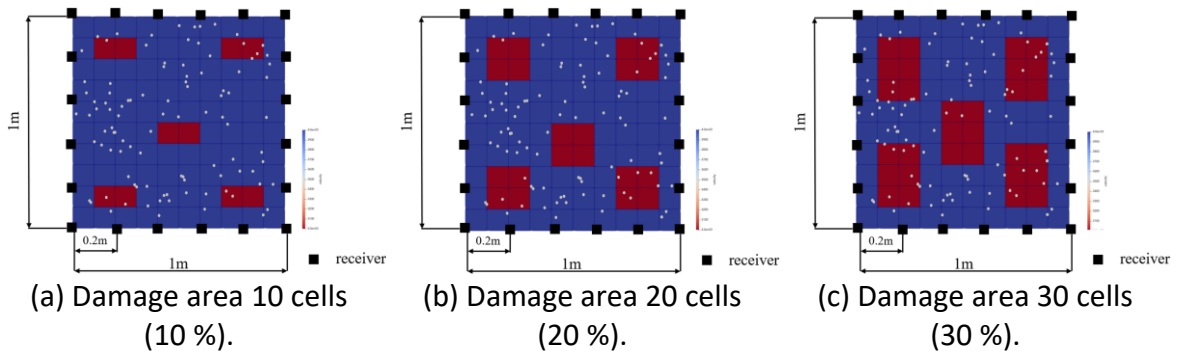
Figure 4.6 Concentrated types of damaged area with different rates of original distribution.

The velocity reconstruction results show in figures 4.7 - 4.12. The red rectangle zones indicate the low-velocity regions that should be identified as the low-velocity regions. From the calculation results, it is denoted that: 1) both algorithms in two damage types can identify the low-velocity region when the damaged area is 10 %, 20 %, and 30 %. Although the value of the low-velocity region identified by LASSO is slightly lower than SIRT, the identification range for the low-velocity region is accurate. 2) for healthy region identification, LASSO performs remarkably well in reconstructing the velocity distribution with few shadows than SIRT in different models.
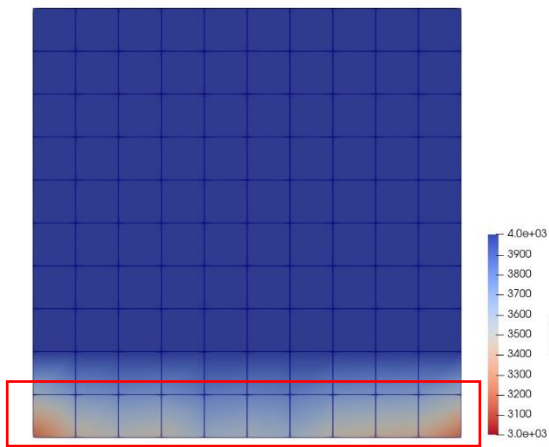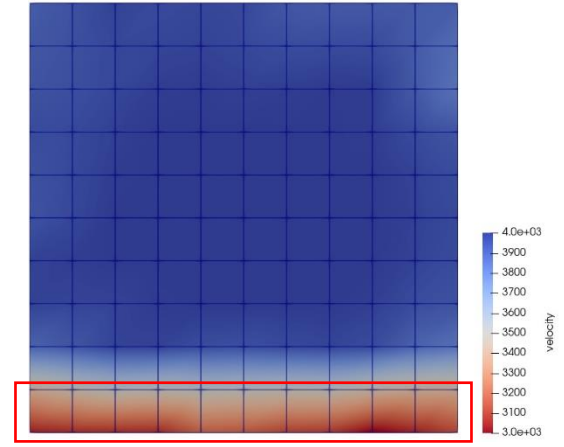
(a) LASSO algorithm.　　　　　　　　　　　(b) SIRT algorithm.

Figure 4.7 Identified results of 10 % defected area.
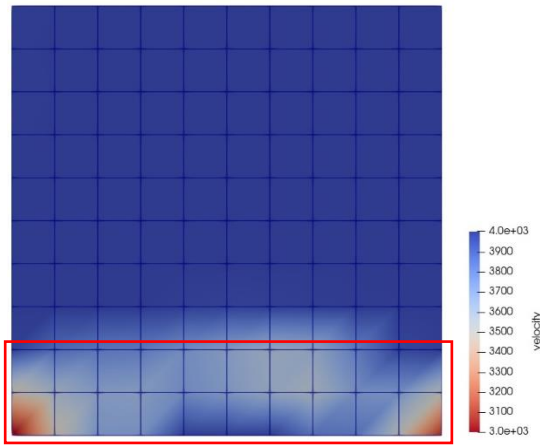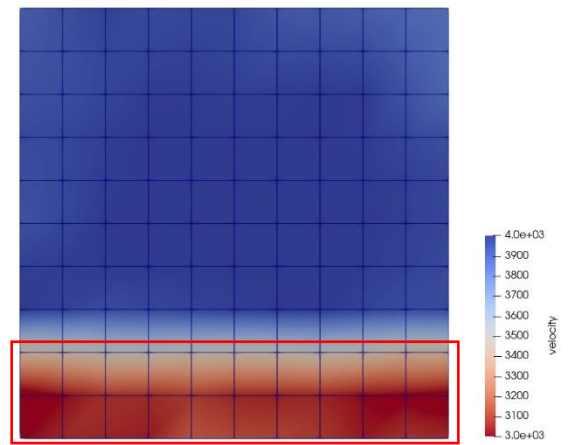
(a) LASSO algorithm.　　　　　　　　　　　(b) SIRT algorithm.

Figure 4.8 Identified results of 20 % defected area.
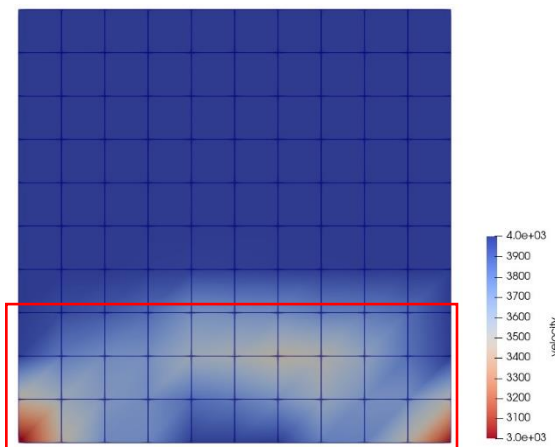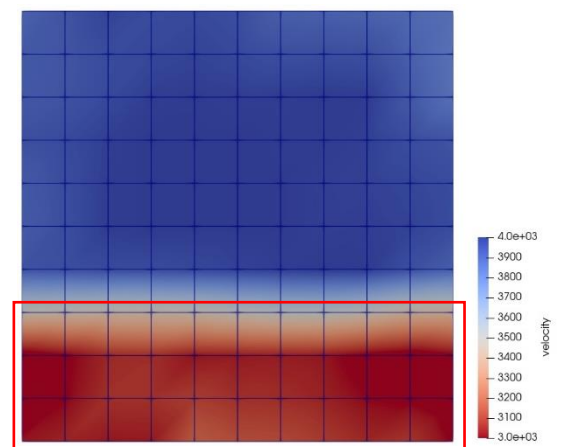
(a) LASSO algorithm.　　　　　　　　　　　(b) SIRT algorithm.

Figure 4.9 Identified results of 30 % defected area.
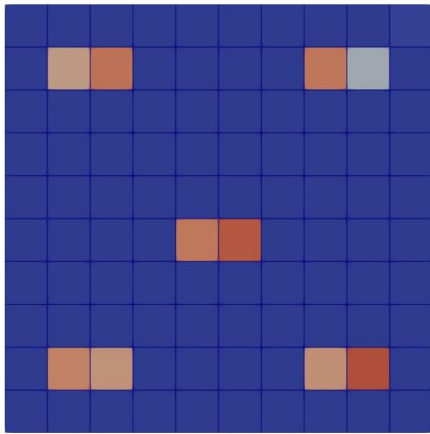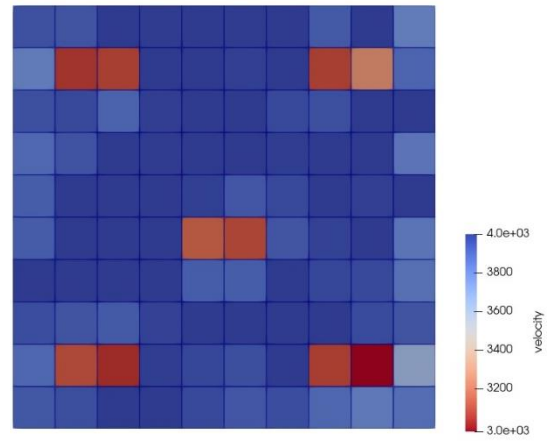
(a) LASSO algorithm.　　　　　　　　　　　(b) SIRT algorithm.

Figure 4.10 Identified results of 10 % defected area.
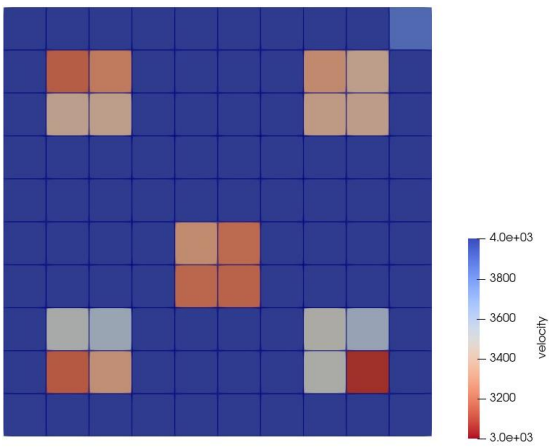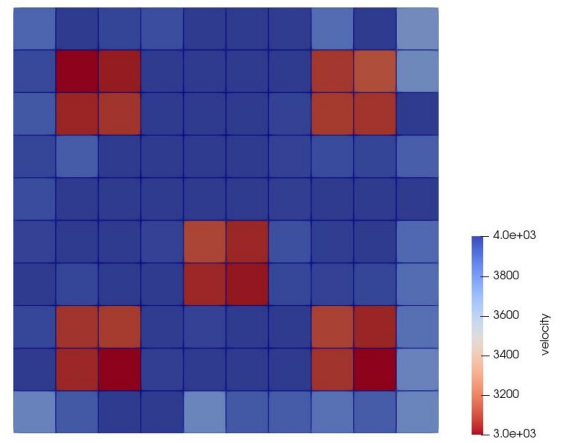
(a) LASSO algorithm.　　　　　　　　　　　(b) SIRT algorithm.

Figure 4.11 Identified results of 20 % defected area.

(a) LASSO algorithm.　　　　　　　　　　　　(b) SIRT algorithm.
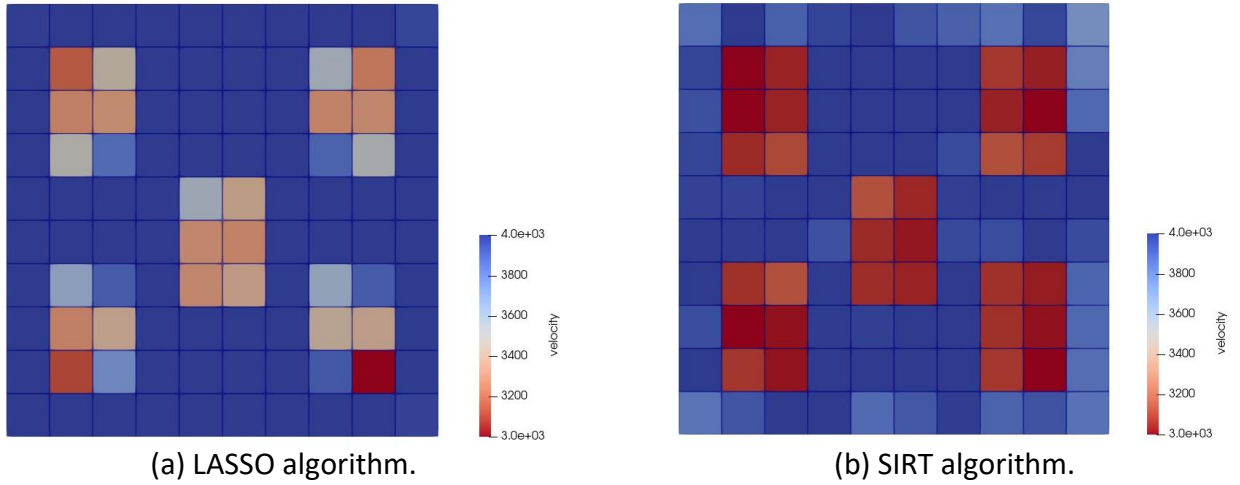
Figure 4.12 Identified results of 30 % defected area.

In the following, the error of strip and concentrated damage type is calculated by the LASSO algorithm for velocity identification in different damage ratios by the difference between the identified velocity results and the original velocity value of each corresponding cell and then calculated by the L2-norm. The L2-norm error of LASSO algorithm trends and calculated values for the two damage types are shown in figure 4.13 (a), and the different percentages of damage area in the healthy part are shown in figure 4.13 (b). The results indicate that the error results of the LASSO algorithm tend to be stable and within an acceptable scope, and the boundary description of the healthy area and the damaged area in the velocity reconstruction image is distinct. The L2-norm error of concentrated low-velocity damaged models is smaller than the strip models after comparing the L2-norm error value of the strip and concentrated damage under different damage ratios using the LASSO algorithm, indicating that LASSO has a better detection ability for concentrated damage types.
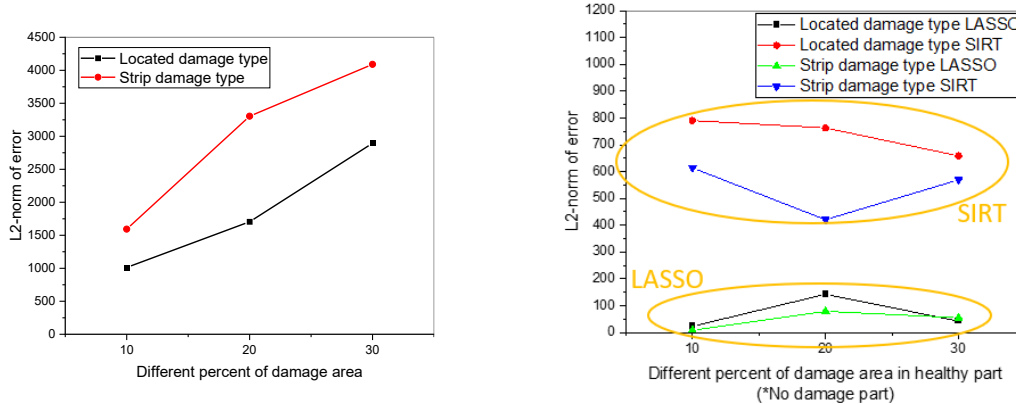
(a) L2 - norm error for LASSO.　　　　　　(b) L2 - norm for healthy part.

Figure 4.13 The error of L2-norm.

4.3 Different types of damage simulation

In order to demonstrate the effectiveness and utility of the proposed damage detection methods in the LASSO algorithm, numerical models were created. Typically, the structural integrity of a concrete structure is compromised by earthquake, fire, collision, or purposeful destruction, as well as structural overloads (such as static overloading), and faults occur. Hole destruction, concentrated holes, and spalling or edge peeling are kinds of concrete failure appropriate for this non-destructive testing methodology via AE tomography as a technique of inspection[57].

The subsequent numerical simulation is based on actual concrete damage patterns, and three distinct damage types were explored to recreate the condition in the basic construction. The velocity of elastic wave propagation in concrete is considered 4,000 m/s, and the standard slowness is calculated based on the velocity. In the following simulation, the blue portion of each model represents the healthy region with a velocity of 4000 m/s, and the red portion represents the damaged area with a velocity of 3000 m/s; the white spheres represent the randomly generated source locations in models. Case 1 is a simulation of the concrete slab shown in figure 4.14 (a) with damaged holes. Figure 8 (b) is a simulation model depicting the size of the model and the position of the receivers. The damaged region is shown by the low-velocity cell. Case 2's damaged region is a concentrated hole, as seen in figure 4.15. The damage is positioned in the model's center and comprises four cells. Case 3 is a simulation of the damage at the edge of the concrete frame, and the simulation model is shown in figure 4.16; the location of the damage is in the upper right corner with lower velocity, and the model consists of six cells for examination. All the models' specific information is presented in table 4.3. Each simulation model's initial elastic wave velocity distribution is uniformly 4000 m/s. The calculating processes remain constant in chapter 4.1.

(a) Damage in real.   (b) Original distribution.
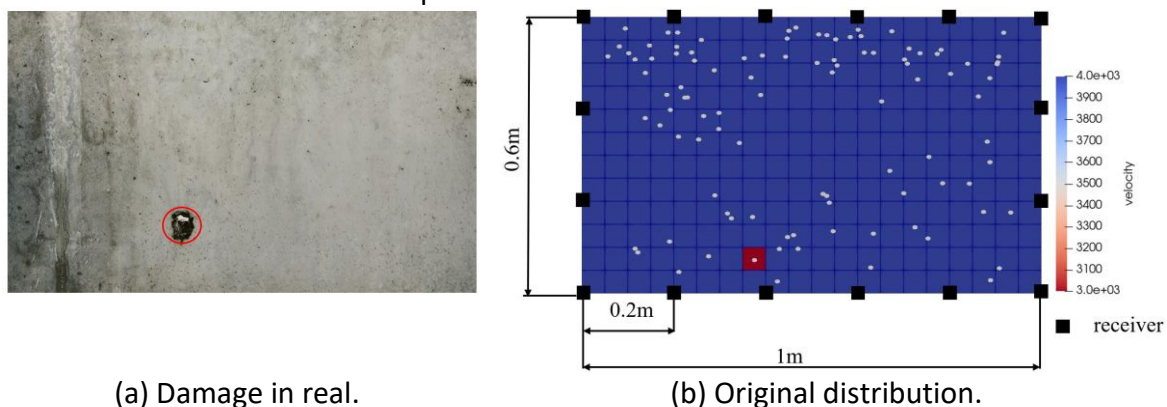
Figure 4.14 Damage target of case 1.
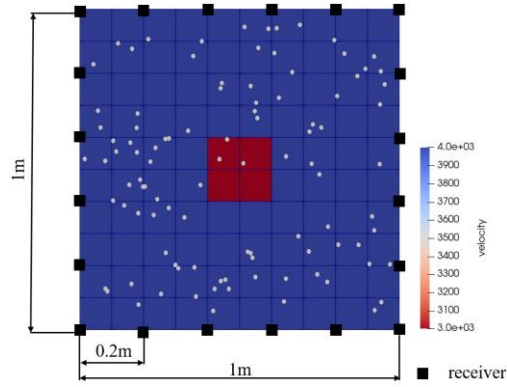
Figure 4.15 Original distribution for damage target of case 2.
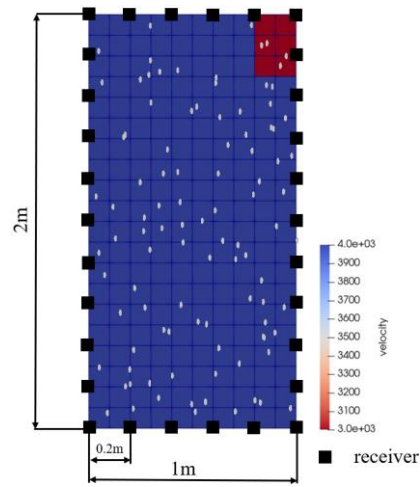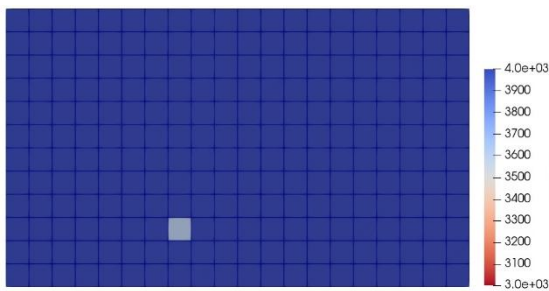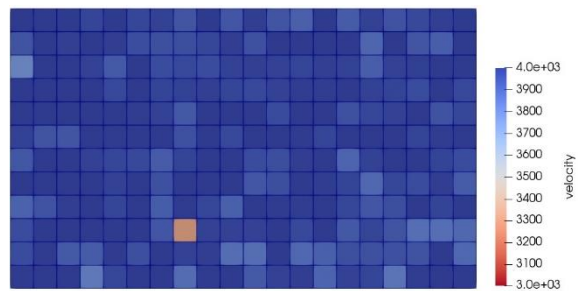

Figure 4.16 Original distribution for damage target of case 3.

Table 4.3 Models information.

CASE	Size of model	Damage area size	Initial velocity	No. of Sensor	No. of mesh	No. of events	No. of relay points	No. of measurement paths
1	1 m × 0.6 m	0.05 m × 0.05 m	4000 m/s	16	240	100	12	1600
2	1 m × 1 m	0.2 m × 0.2 m	4000 m/s	20	100	100	12	2000
3	1 m × 2 m	0.2 m × 0.3 m	4000 m/s	30	200	100	12	3000

(a) LASSO algorithm.

(b) SIRT algorithm.

Figure 4.17 Identified Results of case 1.

(a) LASSO algorithm. (b) SIRT algorithm.
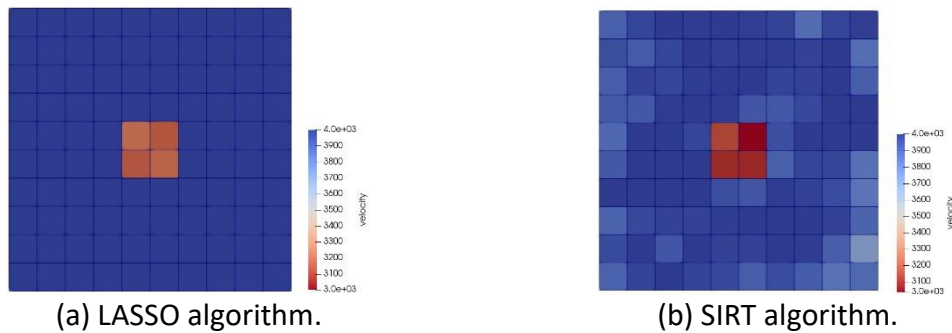
Figure 4.18 Identified Results of case 2.

(a) LASSO algorithm. (b) SIRT algorithm.
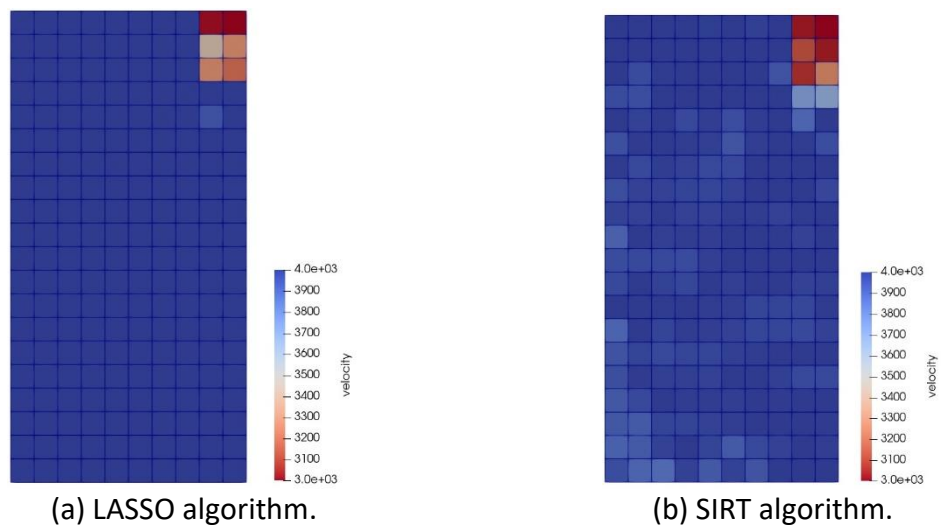
Figure 4.19 Identified Results of case 3.

Figures 4.17 through 4.19 depict the consequences of three distinct simulation models with distinct damage categories. The results demonstrate that the defective region has been appropriately detected. Comparatively to the reconstructed velocity distribution of the SIRT algorithm, the damaged categorization of hole damage, concentrated hole, and edge damage, the LASSO algorithm precisely identified the lower velocity area in every model. Furthermore, the LASSO technique accurately identifies the high-velocity zone of the healthy region in all numerical simulation models, and the discovered velocity distribution has minimal shadows than SIRT. The LASSO method works well for the AE tomography approach for identifying common forms of concrete damage with highly precise reconstructed velocity distribution.

4.4 Three-dimensional (3D) AE tomography

4.4.1 Methodology of 3D AE tomography

The following introduces the methodology of 3D for verification. It is noted that this process assumes the ray path as a straight line based on the homogeneity of the elastic wave velocity distribution. If the specimen is thick enough, the analysis procedure will turn into a pseudo-three-dimensional problem since the ray paths through the specimen will become longer. The theoretical representation of 3D will express as follows: as shown in figure 4.20(a), P is the AE acoustic emission source, and A and S are the receivers. The blue ray segment L$_{PA}$ in Figure 4.20(a) is the ray-trace in the 2D case, represented as L_1, L_2, L_3, and L_4 is the corresponding ray-trace for each meshed cell.

(a) Example of the 3D model.   (b) Calculation of ray path.
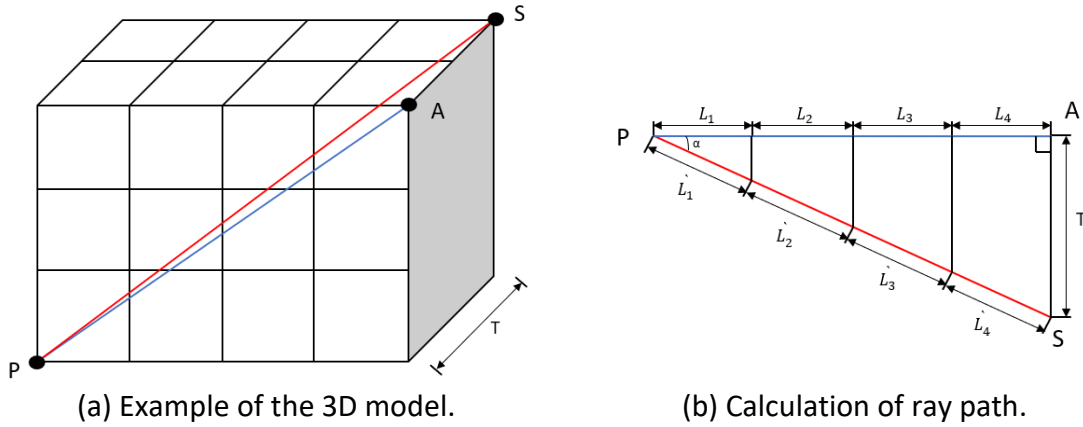
Figure 4.20 Illustration of 3D methodology.

AE tomography could be procedure in three-dimensional space, and the source locations would be identified in the subsurface as well. The most significant difference between 3D and 2D is the factor that increases the thickness T, since every ray-trace changes under the influence of the thickness. If the specimen is thick enough, the acoustic emission ray path may propagate into the subsurface. The acoustic emission ray path will become longer as red ray segment L$_{PS}$, representing the ray trace of each meshed cell on 3D condition, represents the red line segments $\grave{L}_1$, $\grave{L}_2$, $\grave{L}_3$, and $\grave{L}_4$, respectively. Every individual ray trace for AE tomography analysis will be recalculated under this hypothesis[58]–[61]. The method of the calculation can be expressed as follows:

$$\grave{L}_1 = \frac{\sqrt{\left(\sum_{n=0}^{1} L_i\right)^2 + T^2}}{\sum_{n=0}^{1} L_i} \tag{4.1}$$

$$\grave{L}_2 = \frac{\sqrt{\left(\sum_{n=0}^{2} L_i\right)^2 + T^2}}{\sum_{n=0}^{2} L_i} \tag{4.2}$$

$$\grave{L}_3 = \frac{\sqrt{\left(\sum_{n=0}^{3} L_i\right)^2 + T^2}}{\sum_{n=0}^{3} L_i} \tag{4.3}$$

$$L_4^` = \frac{\sqrt{\left(\sum_{n=0}^{4} L_i\right)^2 + T^2}}{\sum_{n=0}^{4} L_i}$$

(4.4)

4.4.2 Numerical simulation of 3D AE tomography

Through the above calculation principles, the 2D problem of AE tomography can be transformed into a 3D problem by increasing the model's thickness to image the inside of the structure accurately. Numerical simulations verify the proposed theory. The thickness of the concrete is 0.25 m, and the size of the failure is 1 m × 1 m × 0.25 m. There are five relay points for each cell. The blue part represents the intact part of the concrete, the red part is the damaged part whose own elastic wave velocity is 3000 m/s. The source location generation is shown in the model above as white dots in figure 4.21, and other relevant model parameters are shown in table 4.4 below.
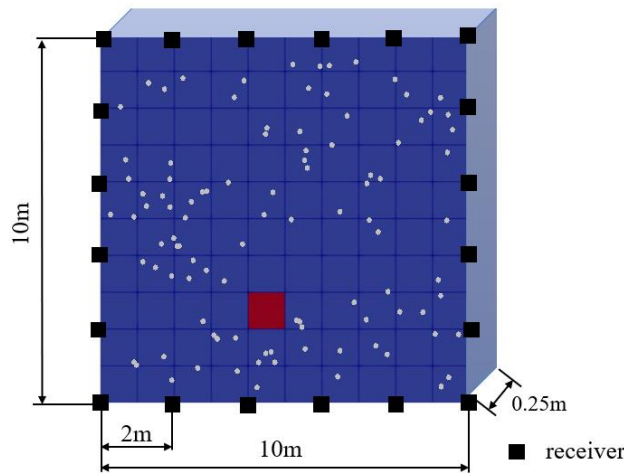
Figure 4.21 Initial velocity distribution of the 3D model.

Table 4.4 Model information.

Size of model	Initial velocity	No. of Sensor	No. of mesh	No. of events	No. of measurement paths
10 m × 10 m × 0.25 m	4000 m/s	20	100	100	2000

After calculating the ray trace by the proposed method, utilize AE tomography to describe the velocity of the internal structure and compare it with the SIRT algorithm for verification, shown in figure 4.22. The results are as follows: The results indicated that LASSO could clearly describe the damage location and size. The traditional algorithm SIRT could also detect the damage information, but the LASSO algorithm can eliminate a lot of the shadow part of the healthy concrete. Thus the velocity distribution image of the LASSO algorithm is more accurate and precise than that of the SIRT algorithm.

(a) LASSO algorithm.　　　　　　　　　　(b) SIRT algorithm.
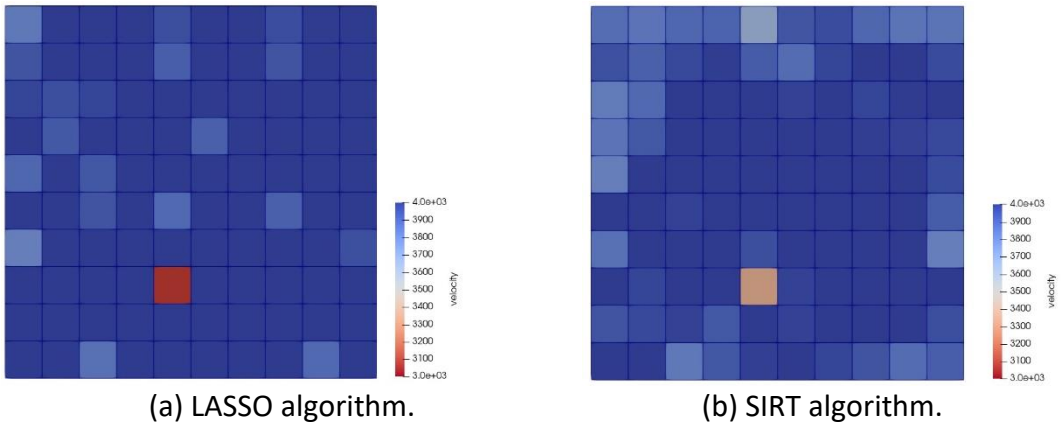
Figure 4.22 3D result of velocity distribution.

5 EXPERIMENT OF AE TOMOGRAPHY

After numerical simulations, the effectiveness and ability of LASSO regression used in AE tomography for velocity distribution have been verified. The first experiment specimen is an aluminum plate, while the second and third experiment specimens are composed of concrete. These experiments are designed to validate the proposed method in practical works, and the result of the SIRT is adopted to compare the AE tomography technology.

5.1 Aluminum plate experiment

5.1.1 Overview of specimen

The specimen is a 1 m × 1 m × 0.005 m aluminum plate with an artificial flaw consisting of a 0.5 m × 0.04 m slit in the specimen's bottom right corner. It is observed that this specimen is treated as a two-dimensional plate since its thickness is tiny relative to its size. At the same time, the source of acoustic wave emission and the sensors were placed on the same side of the specimen. The acoustic wave might propagate as a polygonal line in the subsurface of the specimen because the diffraction phenomenon may occur. However, the error of measurement paths from acoustic source to receivers is minimal since the thickness is thin. The velocity of propagation of elastic waves in the specimen is 5500 m/s. As shown in figure 5.1, nine sensors are spaced 0.4 m apart around the specimen and one is situated in the middle of the specimen. In each sensor, the recording threshold, the preamp amplitude, and the bandpass filter are respectively set to 50 dB, 60 dB, and 1 kHz to 1 MHz. Therefore, the arrival time is accurate to six decimal places. 72 source sites are shown as white spots with a 0.1 m spacing and uniform distribution in the model, as seen in Figure 5.1 (b).

(a) Photograph of the specimen. (b) Schematic diagram of the specimen.
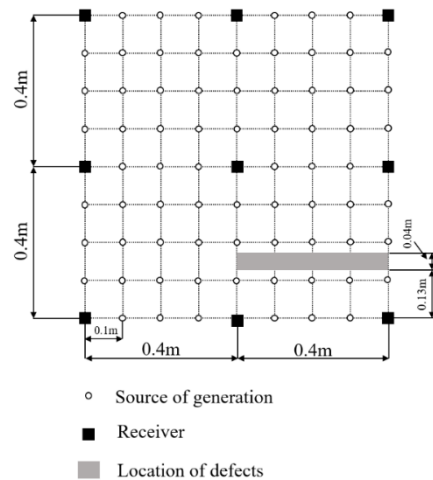
Figure 5.1. Overview of specimen.

The LASSO inspection procedure for AE tomography is as follows: (1) The application of the elastic wave created by breaking the pencil lead at each source point, as shown in Figure 5.2 (a). Using the length of 3 mm and hardness of 2H pencil lead, the 72 setting places are broken to emit the events, and nine sensors receive the elastic wave accordingly, which is then transmitted to the acquisition system and amplified to produce the detected measured AE wave[62]. In this situation, the noise and signal components of the AE events wave can be differentiated clearly. (2) The arrival times are selected at the end of the noise part of each measurement path. Notably, the relay point component splits each mesh cell edge into seven sections, giving in 60 relay points per mesh. The model is meshed by squares with a length of about 0.13 m, meaning that there are 36 (6 × 6) cells in total. (3) Since the amplitudes of the signal and noise components fluctuate considerably, the travel time between source sites and sensors could be extracted from the related time history to reconstruct the elastic velocity distribution. (4) The model's internal velocity distribution is defined by the differential slowness vector Δs in equation 2.13, and the slowness distribution is updated using Δs.
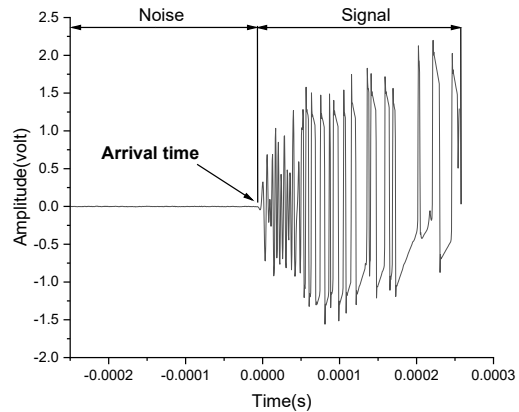
(a) Pencil leading.   (b) Example of the measured signal.
Figure 5.2 Measurement event generated and data collected.

5.1.2 Results of experiment

The reconstruction of velocity distribution by SIRT and LASSO algorithm is tried to verify the proposed algorithm with different numbers of events. The number of events of 9, 18, 27, 36, 45, 54, 63, and 72 is selected, and related occupations of the entire event and measurement paths are shown in figure 5.3.

Event No. /measurement path No.	Select events	SIRT result	LASSO result
9/ 81 paths			
18/ 162 paths			
27/ 243 paths			
36/ 324 paths			
45/ 405 paths			
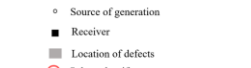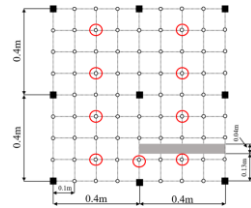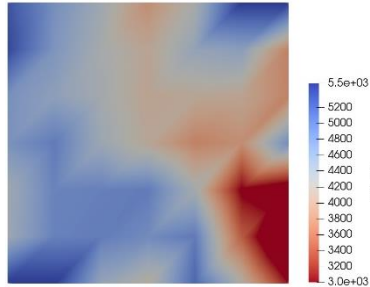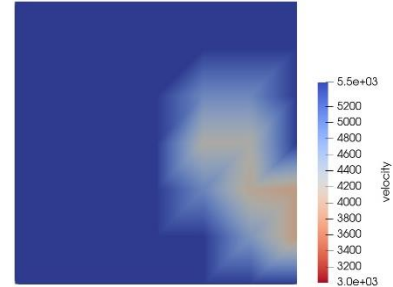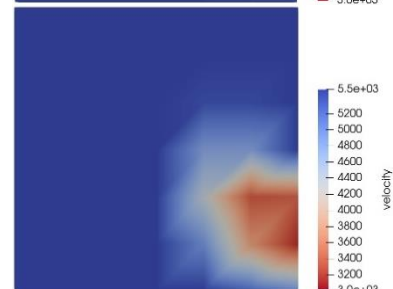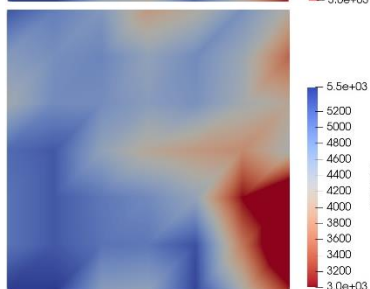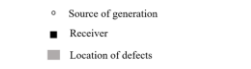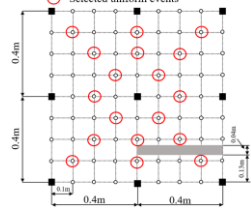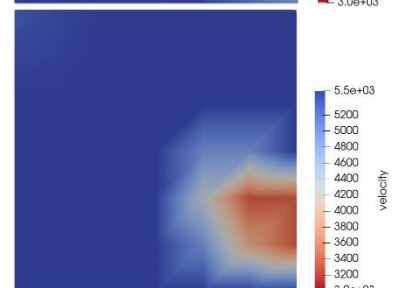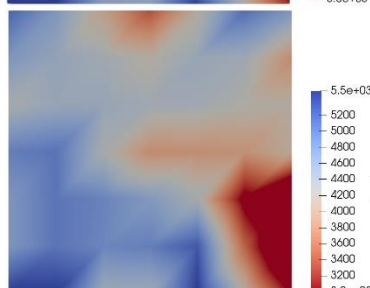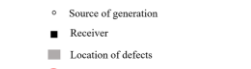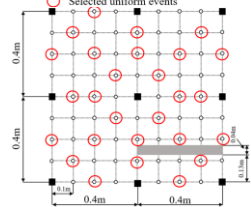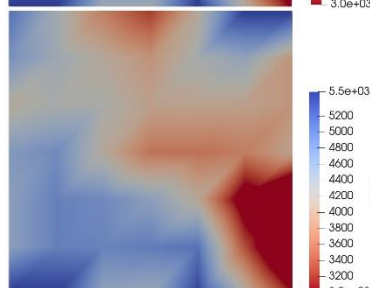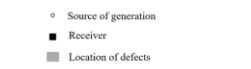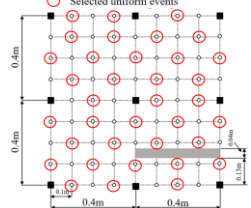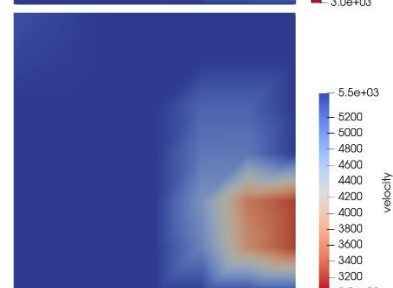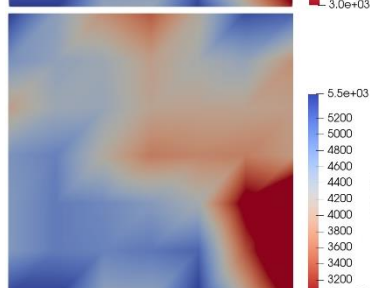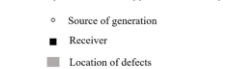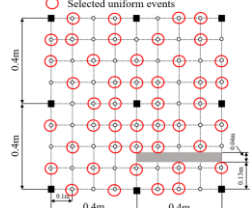
Figure 5.3 Different number of events for velocity distribution result by LASSO and SIRT algorithm.

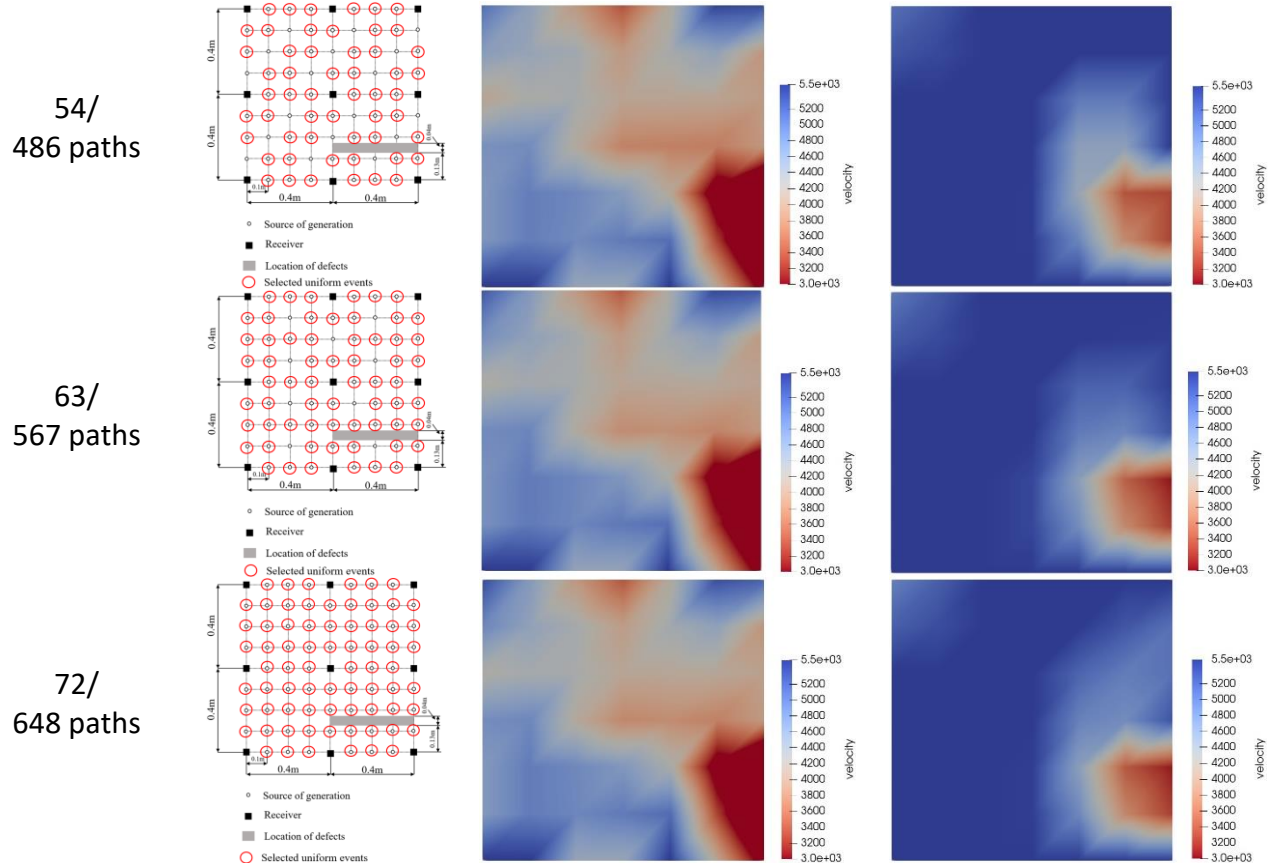The red circle is the event selected on the model, and the selection is as uniform as possible to ensure for making the reconstructed velocity distributions are relatively accurate. In the reconstructed results, the red part is the damaged area with a velocity lower than 3000 m/s distribution, and the higher velocity (5500 m/s) part is a healthy condition displayed as both algorithms detected as the blue area. The reconstructed elastic wave velocity distribution results of the LASSO using 18 events (25 % of the total) with 162 measurement paths begin to stabilize according to figure 5.3. Although events and measurement paths increase later, the results do not change much, and the velocity distribution can be clearly described; While SIRT uses 36 events (50 % of the total) with 324 measurement paths, the results become stable as well. Although the events and paths increase, the results maintain the same trend, as shown in figure 5.3.

(a) Result of LASSO adopting 18 events.   (b) Result of SIRT adopting 36 events.
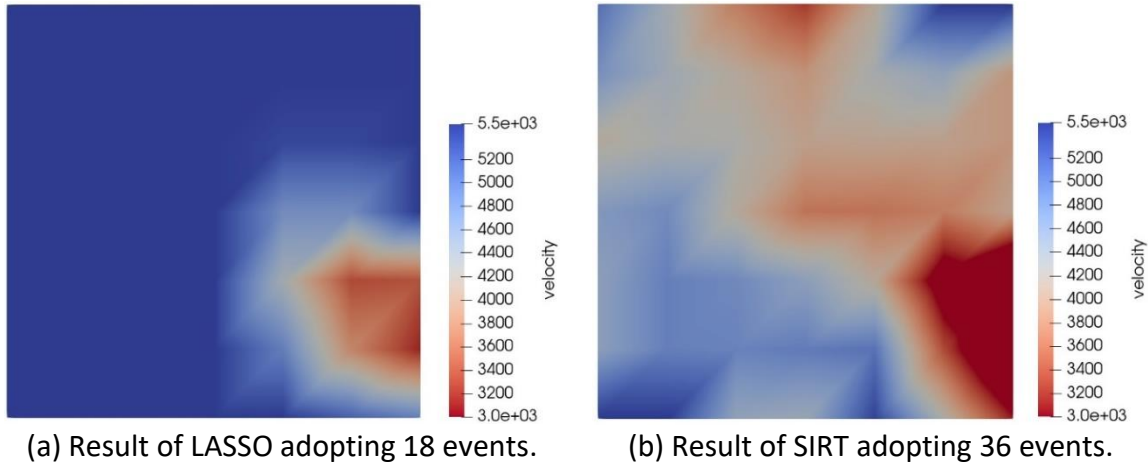
Figure 5.4 Reconstructed velocity distribution.

According to figure 5.4, the result of identified velocity distribution by LASSO is consistent with SIRT, which validates that the proposed method identified critical damage results accurately through a smaller number of event data in AE tomography. It is essential that the LASSO algorithm could more accurately restore the range of defects using a smaller number of samples, which have 18 events data instead of 36 events data adopted by the SIRT algorithm. The flow chart and image of measurement paths for two kinds of algorithms are shown in figure 5.5. The more important point is that the LASSO results can effectively eliminate the shadows part in the reconstructed velocity distribution image and catch a more comprehensive extensive low-velocity range and describe the edge of the damaged area with more precision, which means the result of the velocity tomography is more precise and distinguishable than the result of the SIRT algorithm.
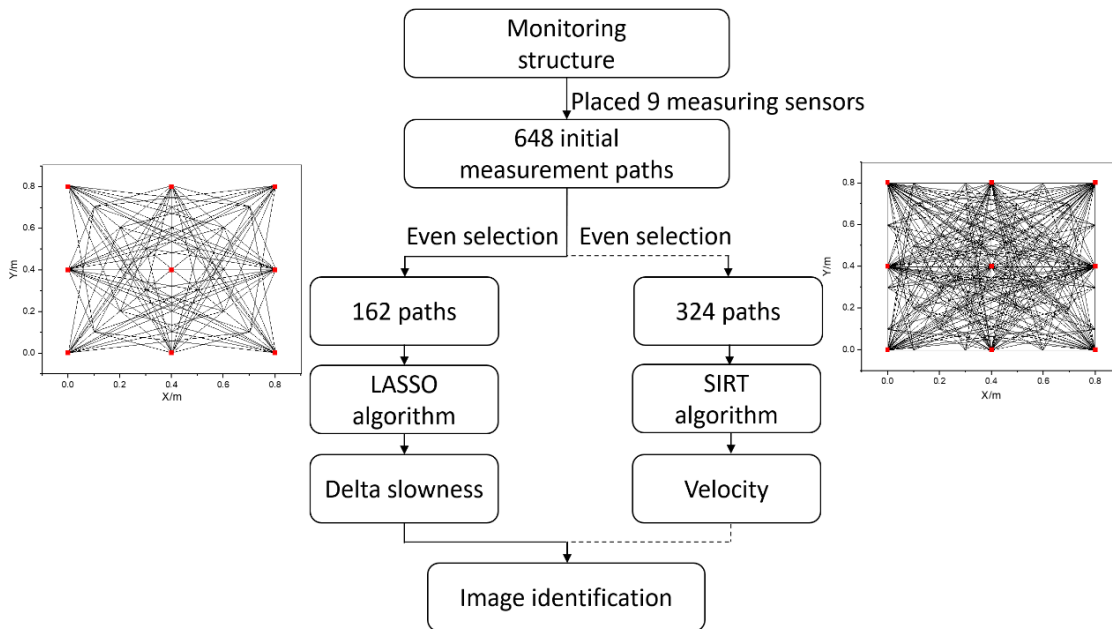
Figure 5.5 Flowchart of AE tomography in different imaging methods.

In this experiment, because the defect of the specimen is exceptionally narrow and long instead of sparse and scattered distribution, the elastic emission wave will bypass the defected part and then reach the receivers during the transmission process according to the basic theory of ray-trace technique in AE tomography. The velocity on the left side of the defected area was displayed as a significantly high-velocity distribution because the real ray paths through this area are crossed with a length close to that through the non-defected area, rather than theoretically through the defective area, as shown in figure 5.6.
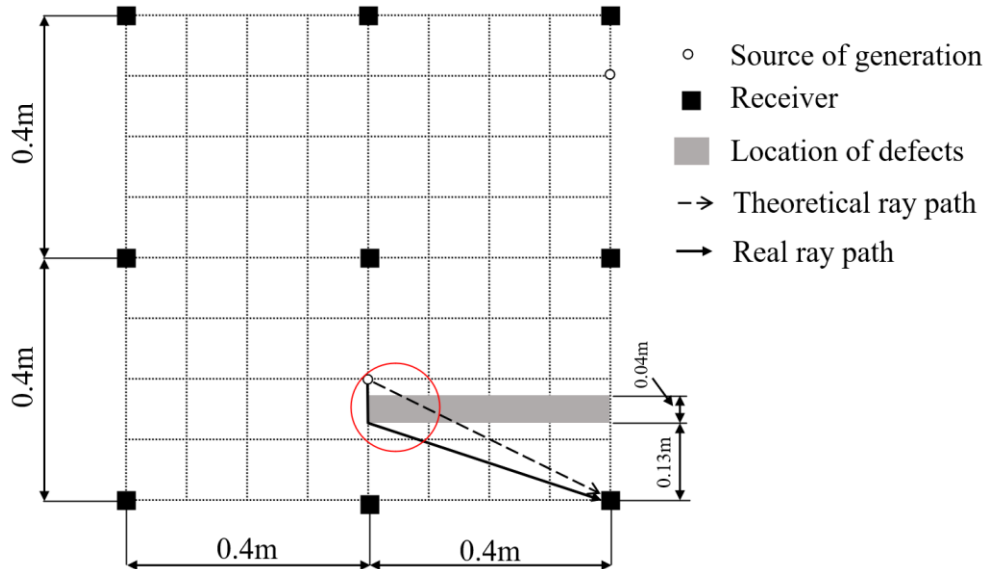

Figure 5.6 The left side of the defect area with high velocity in velocity distribution.

On the contrary, the elastic emissions wave needs to bypass the entire defective part to reach the receivers with long-distance propagations on the right half of the model, resulting in a low-velocity range in the right half since the wave propagation time increases. In AE tomography technology, the exact elastic wave emission position is unknown, it needs to estimate time and the source location and then identify the velocity distribution. As a consequence, AE tomography is a technique that can detect the realistic condition of velocity distribution for defect area identification in the real world.

5.2 Concrete slab experiment

5.2.1 Experimental overview

For reinforced concrete constructions such as bridges, the passing sheath tube is commonly filled with grouting material to protect the PC cable and prevent the intrusion of external deterioration factors. If the passing sheath tube filling is insufficient, impurities like rainwater will enter the sheath, causing the PC steel material to corrode, and breakage may

significantly degrade bridge performance. It is not easy to find out through simple inspections such as naked eye observation and judging by knocking sounds. An unfilled sheath part in the specimen represents the internal defects of the prestressed concrete member. This experimental study is implemented to verify the new algorithm by comparing it with the traditional algorithm SIRT to judge the internal condition of the concrete component.

5.2.2 Specimen overview

The specimen in this experiment is a concrete slab with a size of 1200 mm × 1200 mm × 250 mm and a weight of 830 kg. A hollow plastic tube with a diameter of 63 mm is in the middle part of the test piece. The specimen is shown in figure 5.7.

Figure 5.7 Overview of the concrete slab specimen(This picture is from iTECS technical association).

Since the front of the specimen needs to receive the emitted AE elastic waves, the sensors are arranged at the rear of the specimen. There are six sensors, and the distance between the left and right sides is 1000 mm, and the distance between the upper and lower interval is 500 mm, respectively. The experimental arrangement is shown in figure 5.8.
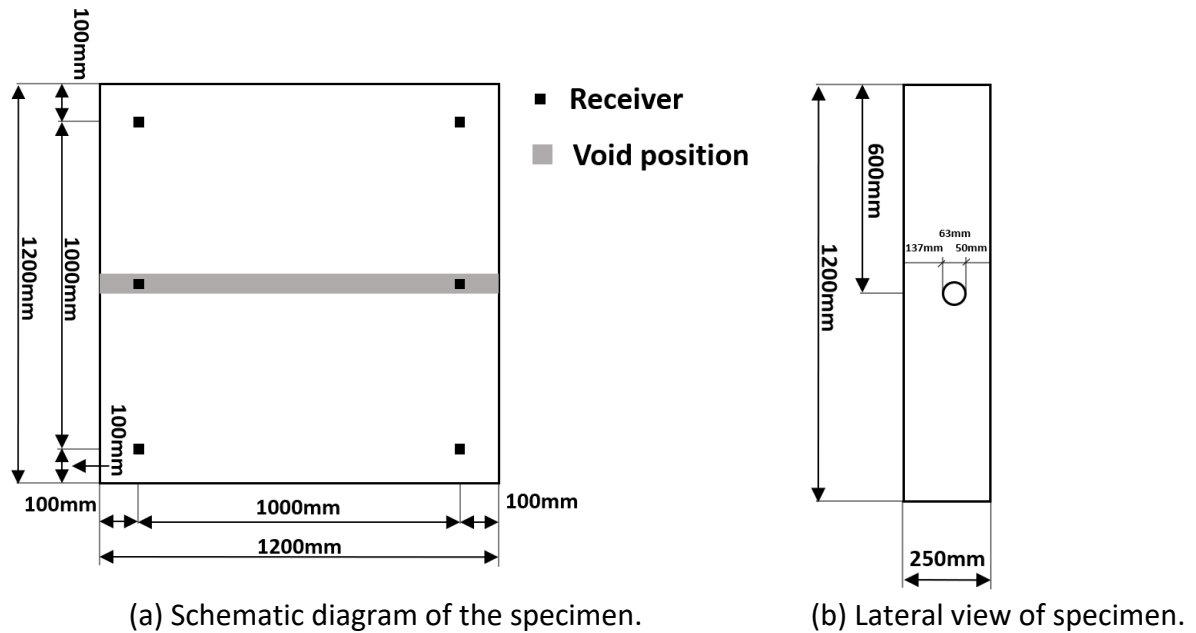
(a) Schematic diagram of the specimen.　　　　　(b) Lateral view of specimen.

Figure 5.8 Specimen geometry.

5.2.3 Elastic wave emission

In this experiment, the elastic wave is emitted by hitting the front surface of the concrete specimen with plastic bullets fired by an air gun. The air gun is in full auto mode when firing bullets to create elastic waves, and the bullets at full auto shooting speed are 850 /min. Thus, each bullet was shot at an approximated interval of 0.07 s. Every bullet is spherical with 6 mm diameter and the weight is 0.2 g, as shown in figure 5.9 (b). Shoot the front side of the specimen as uniformly as possible to ensure uniform distribution of events at a distance of 5m from the specimen to emit elastic waves, as shown in figure 5.9 (a). It is noted that this experiment was conducted in an open space outdoors since the air gun will generate noise largely when firing bullets, which affects the clarity of the AE wave signal collected by sensors.
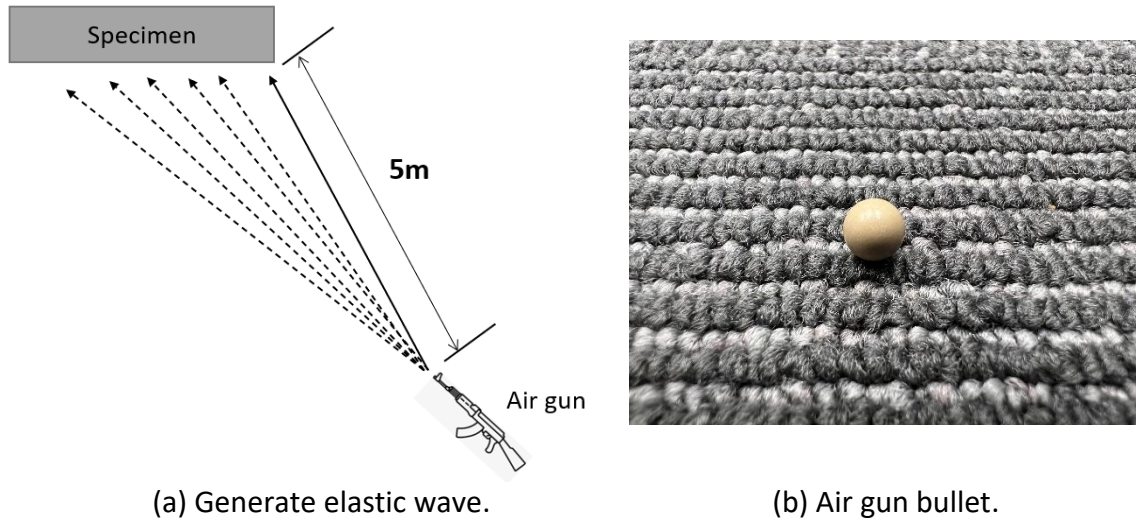
(a) Generate elastic wave.   (b) Air gun bullet.
Figure 5.9 Method of elastic wave generation.

5.2.4 Calculation process

1) Extract the arrival time from the collected data. The interval time between each event is especially short due to the rate of fire speed being extremely fast and easy to generate repercussions as interference data. Thus, it is very difficult to determine whether or not the collected arrival times by different sensors are from the same group. The data is identified according to the principle that the three decimal places of the collected arrival times should be approximately consistent with the propagation velocity of elastic waves in concrete. The noise and arrival time parts can be clearly separated from the collected valid elastic wave data. After analysis and comparison, 721 groups of detected events were identified from the recorded valid monitoring data. There are six sensors to receive elastic waves, and the number of measurement paths is 4326 (721 × 6 = 4326) in total.

2) Calculate and analyze the collected arrival times. The initial velocity is set at 4000 m/s, which is consistent with the propagation velocity of elastic waves in intact concrete. The number of mesh cells in the calculation model is 16 squares, the side length of each square is 250 mm, and there are 60 relay points in each cell. This density of relay points not only ensures accuracy but also maintains economic computing resources.

3) The velocity distribution is reconstructed by the traditional SIRT and LASSO algorithms for verification, respectively.

5.2.5 Result of concrete slab experiment

This study explores the practicability and evaluation ability of the LASSO algorithm to work on AE tomography through concrete specimens embedded with unfilled sheaths. Although this experiment does not fully detect the defective low-velocity area, the edge of the

vacancy part in the specimen was found, and a deeper understanding of AE tomography in the concrete specimen is summarized as follows:

The results are shown in figure 5.10. The blue area has higher velocity, representing the specimen in the soundness condition. The red area has lower velocity, which means damage condition. The defect part in the specimen was not able to clearly spot form velocity distribution neither the SIRT nor LASSO algorithm. Although not all the damaged areas are wholly detected, two kinds of algorithms have the same tendency in the result. AE tomography has limited ability to detect if the concrete specimen is relatively thick and the defective area is elongated and encased in the center position. The description of the low-velocity areas at both edges is apparent, and it can be seen that the LASSO algorithm is clearer than traditional SIRT algorithm.

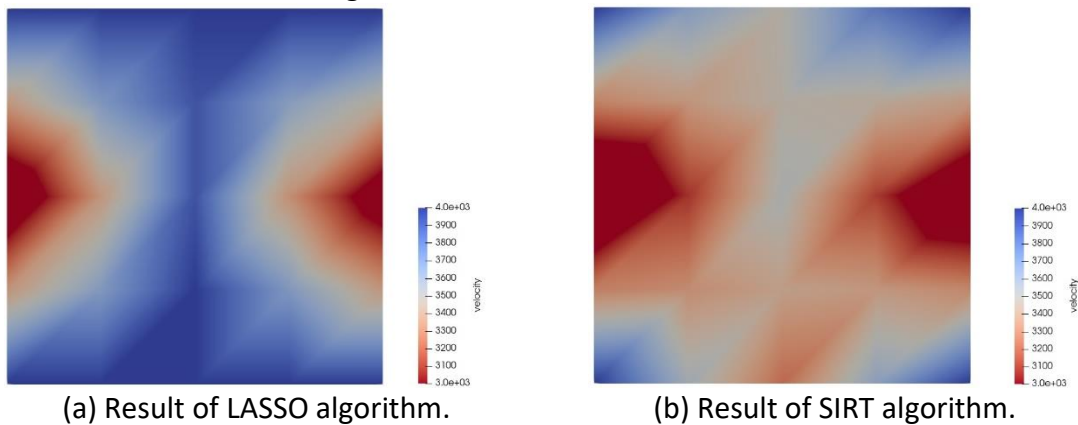(a) Result of LASSO algorithm.   (b) Result of SIRT algorithm.

Figure 5.10 Concrete slab velocity distribution result.

The reasons why the defected area cannot be detected entirely are analyzed as follows: The elastic wave will be emitted when the BB bullet hits the surface of the specimen. Since the concrete specimen is relatively thick, it is difficult for the elastic wave to spread as expected, penetrating the cavity area like a straight line. However, the elastic wave might go through the defective low-velocity area as a polyline because of refracting before reaching the receivers. Therefore, the defective area showed high velocity and was hard to distinguish.

5.3 Reinforced concrete prefabricated retaining plate experiment

5.3.1 Overview

The following experiment detects the concrete prefabricated retaining plate to study and verify the effectiveness of the proposed algorithm. The specimen is a reinforced concrete prefabricated retaining plate, which is in accordance with the JIS standard. The schematic diagram of the specimen is shown in figure 5.15. The specimen has a length of 910 mm, a height of 300 mm, and a width of 60 mm. The primary reinforcement and all secondary reinforcement are all D6 deformed steel bars. The concrete has parameters as follows:

design strength is σ_{ck} 30.0 N/mm², the slump 15.0 ± 2.5 cm, the standard deviation is σ 2.00 N/mm², the cement ratio is 48.0 %, the composite strength is σ_c 36.0 N/mm², and the fine aggregate content 43.0 %. The defective area is in the middle as a circle with a diameter in 106 mm and throughout the whole specimen.

(a) Front of the specimen.   (b) Lateral specimen.

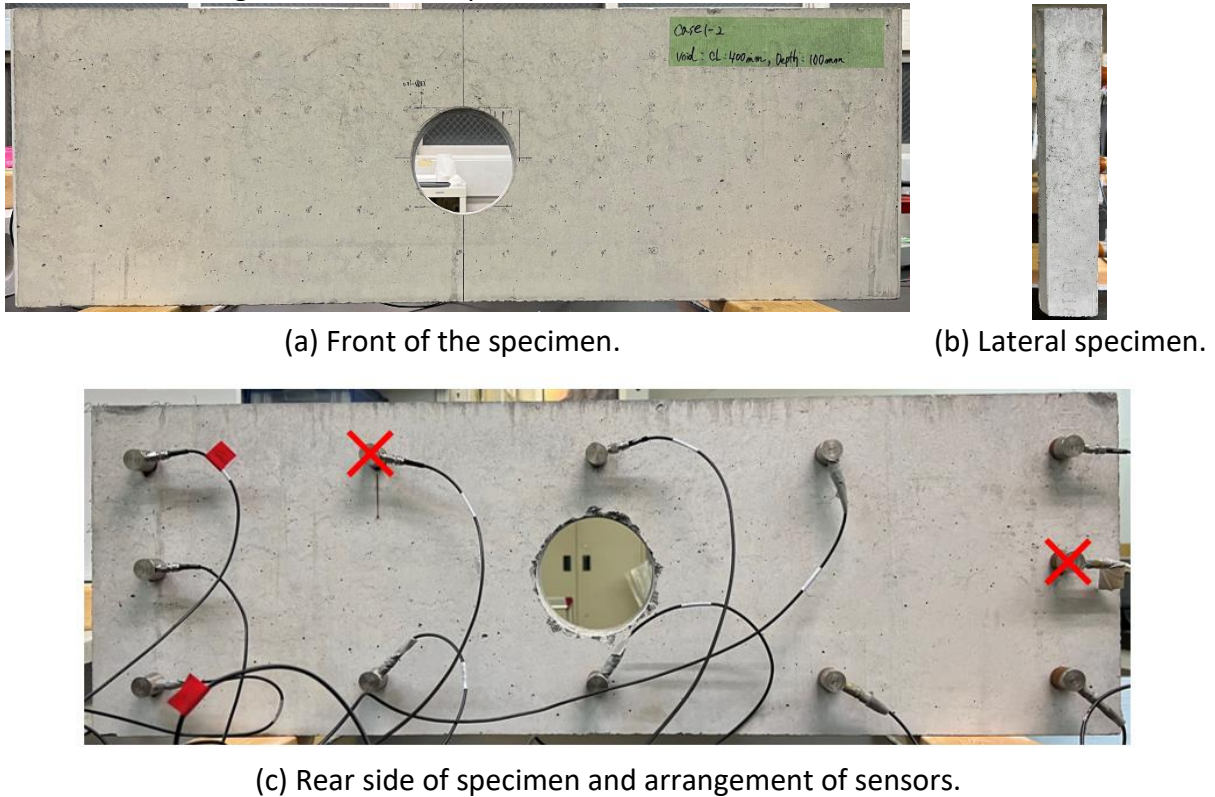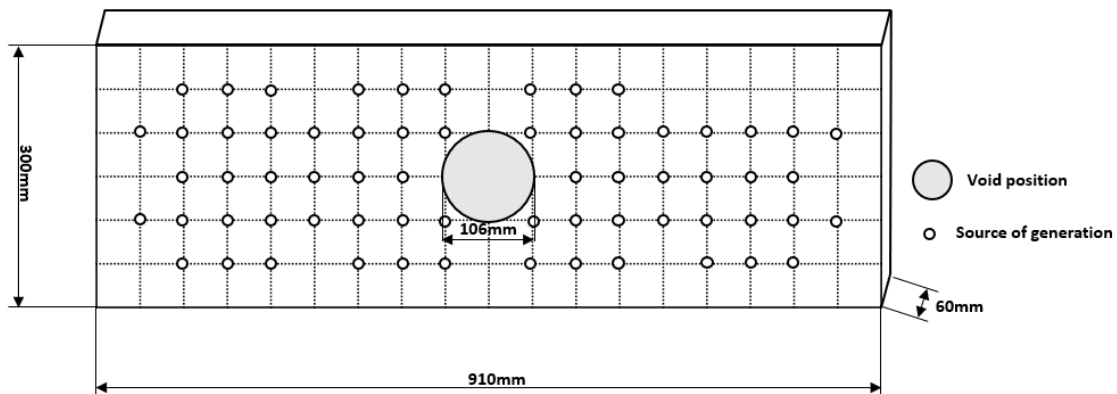(c) Rear side of specimen and arrangement of sensors.

Figure 5.11 Specimen overview.

5.3.2 Experiment procedure

There are 10 sensors in total (In the planning of the experiment, 12 sensor data were collected in the initial measurement, but only 10 sensor data were used due to 2 sensors' data being abnormal.), which are arranged on the back side of the specimen. The abandoned sensors are shown as red crosses (×) in figures 5.11 (c) and 5.12 (b). The distance between the three sensors on the left and right edge is 10 mm, and the distance between the horizontal sensors is 20 mm, as shown in figure 5.12 (b). According to the test for this experiment, the threshold for each sensor is 45 dB will be suitable and sensitive enough to catch the signal accurately. Therefore, the accuracy of the arrival time is six decimal places.

(a) Arregrment in front of the specimen.
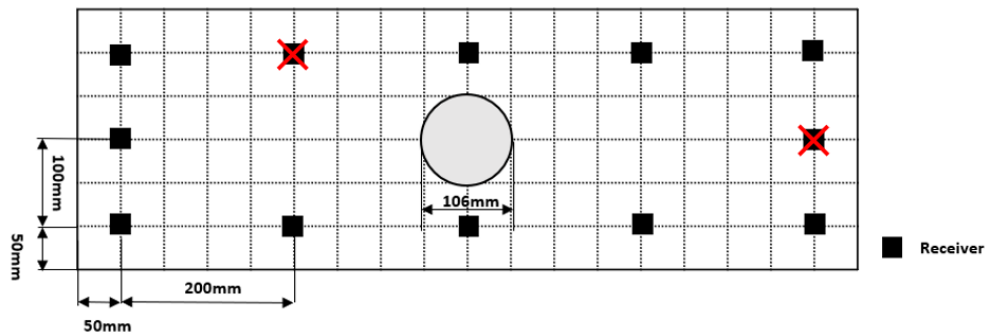
(b) Sensors arrangement on the rear side of specimen.

Figure 5.12 Schematic diagram of the specimen.

5.3.3 Calculation steps

1) This experiment used pencil lead breaks to emit elastic waves one by one on the concrete specimen surface at the points with a total number of 65 where the source generation was arranged in advance, as shown in figure 5.12 (a). The hardness of the pencil lead is 2H and the length is 3 mm, which keep the same as the aluminum experiment, as shown in figure 5.13. Each emitted elastic wave is separately received by each of the 10 sensors on the back of the specimen.

Figure 5.13 Pencil lead breaks.

2) The arrival times are extracted separately from the collected elastic waves. The collected elastic waves can clearly distinguish between the noise and signal parts to obtain the arrival time.

3) In the third step, it is necessary to formulate the calculating model and check the collected arrival times to prepare for velocity distribution analysis. The total number of measurement paths is 650 (calculated as 65 events × 10 sensors = 650), the initial velocity is set to 4000 m/s, and the total number of cells in the calculation model is 64 (16 × 4 = 64). The size of each element is a square with a side length of 0.05 m, and there are 60 relay points in each cell. The number of relay points is defined to ensure accuracy and economical computing resources.

4) The final calculation step used the SIRT algorithm and proposed method LASSO to reconstruct the velocity distribution, respectively.

5.3.4 Experiment result

This study uses a reinforced concrete prefabricated retaining plate to validate the proposed algorithm experimentally. Through the collection of elastic waves by sensors, the component damage is described by velocity reconstruction, and the calculation results of the traditional SIRT algorithm and the LASSO algorithm are compared for verification. The conclusions are as follows:

As shown in figure 5.14, the blue region is the healthy non-defective concrete part expressed as the high-velocity area; the concrete hole part represents the low-velocity area. Both algorithms can describe the damaged area. The image reconstructed by the LASSO

algorithm can more clearly describe the boundary of the defective zone. Since the concrete in the healthy area has few prominent shadows, that is the reason why the reconstructed velocity distribution is more explicit. It is indicated that the LASSO algorithm can reconstruct the image more clearly than SIRT algorithm. It is confirmed that the LASSO algorithm can evaluate the position of the concrete cavity and can be applied to the non-destructive testing of concrete.
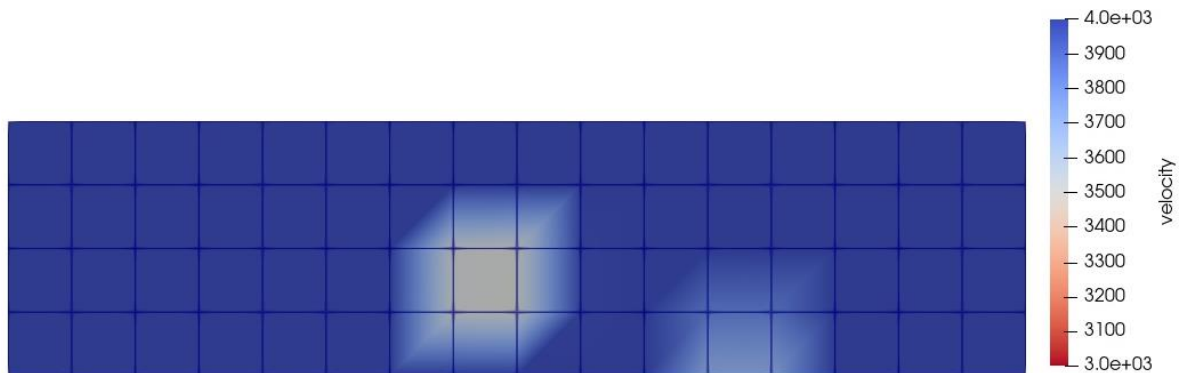
(a) Result of LASSO algorithm.
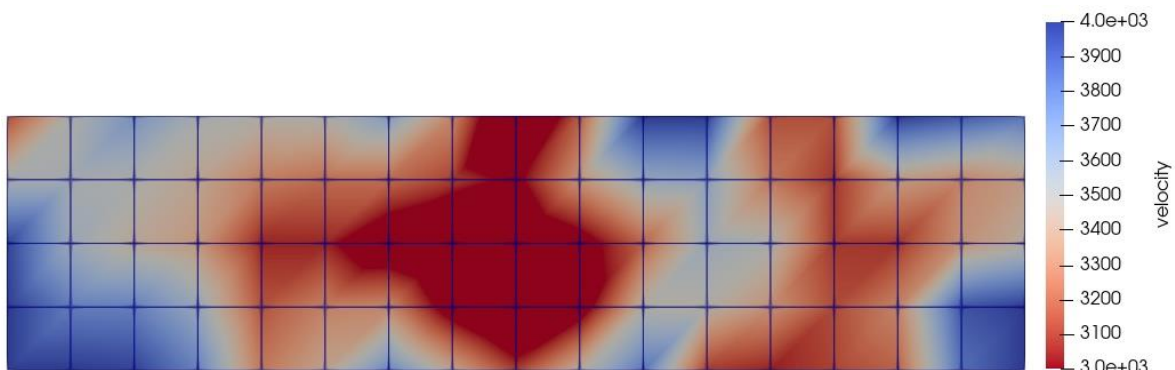
(b) Result of SIRT algorithm.

Figure 5.14 Reconstricted velocity distribution.

It is noted that the residual error between observed and calculated travel times should be zero in intact microstructure theoretically because the distance between event point to receivers and velocity on homogeneity medium is identical. However, there is a discrepancy between the observed and theoretical travel time of the elastic wave propagating the unbroken region in the experiment due to the existence of refraction and diffraction.

The algorithms of SIRT calculate each divided element iteratively, the intact mesh cells are affected during the iteration, which is why the flawless part appears as shadows in elastic velocity distribution. However, in the LASSO algorithm, these entire areas are occupied by the majority of the model that the travel time residual is also described as infinitely close to zero. It is remarked that the intact part is affected very little during the calculation; hence

the original velocity distribution in the intact part is almost maintained. In the calculation involving the defect area, which describes as low-velocity cells, due to the influence of lambda in equation 2.13, lambda is the regularization parameter and equal to calculate extreme value under the constraints in the function. The damaged area described as low-velocity regions in the velocity reconstruction is sharpened and pronounced. Compared with SIRT, the LASSO algorithm could identify the more distinguishable elastic velocity distribution since the optimal local solution is solved subject to a minimum sum of residual errors that are not zero.

6 CONCLUSIONS AND PROSPECT

This research proposed a novel algorithm based on LASSO to overcome the problems existing in the traditional non-destructive testing technology AE tomography.

In order to verify the validity and applicability of the new algorithm, numerical simulation and actual experiments were carried out to study the calculation conditions and the ability to detect internal defects. After this research, there is a deeper understanding of the evaluation ability and superiority of the LASSO algorithm applied to the AE tomography technique, and the main conclusions are as follows:

1) The application of compressive sampling (CS) provides a new algorithm for elastic wave tomography (EWT), which uses fewer paths and obtains the same accurate velocity reconstruction results as the traditional algorithm SIRT. After randomly selecting the elastic wave testing during the measuring step and reconstructing the computation by CS, precise velocity distribution results equivalent to SIRT algorithm are achieved. The compressive sampling method uses fewer measurement paths than traditional SIRT algorithm, which drastically decreases the number of calculations while maintaining the same accuracy. The results show that this method can accurately locate the position of concrete injury and detect the degree of damage with extraordinary efficiency.

2) According to the study by numerical simulation of the LASSO algorithm in AE tomography, it is suggested that the value of lambda suitable for AE tomography should be less than 0.2, preferably less than 0.09, and the specific value should be modified according to different models.

Moreover, the numerical simulation models of the strip and concentrated damage types were calculated under the damage ratios of 10 %, 20 %, and 30 %, respectively, and compared with the traditional algorithm SIRT. The L2-norm error calculation was carried out with the type of concentrated damage. It is essential that LASSO algorithm has an accurate detection ability for less than 30 % of the type of concentrated damage, which could describe the damaged area and identify low-speed areas. Furthermore, for the healthy region of reconstructed velocity distribution, LASSO performs remarkably well in reconstructing the velocity distribution with few shadows than SIRT. The LASSO algorithm accurately identifies the high-velocity area of the healthy region with tinny shadows. The LASSO method works well for the AE tomography approach for identifying common forms of concrete damage with exact reconstructed velocity distribution.

3) According to the result aluminum plate experiment, the result of identified velocity distribution by LASSO agrees with SIRT algorithm, which validates that the proposed method identified critical damage results accurately through a smaller number of event

data in AE tomography. It is essential that the LASSO algorithm could more accurately restore the range of defects using a smaller number of samples, which have 18 events data instead of 36 events data adopted by the SIRT algorithm. It is vital that the LASSO effectively eliminate the shadows part in the reconstructed velocity distribution image, and catch a more comprehensive extensive low-velocity range correctly, which means the result of the velocity tomography is more precise and distinguishable than the result of the SIRT algorithm.

The concrete experiment indicated that AE tomography has limited ability to detect if the concrete specimen is relatively thick and the defective area is elongated and encased in the center position.

The experiment of prefabricated retaining plate indicated that the image reconstructed by the LASSO algorithm could more obviously describe the boundary of the defective area. Since the concrete in the healthy area has no prominent shadow. The results show that the LASSO algorithm could reconstruct the image more clearly than the SIRT algorithm. It is demonstrated that the algorithm can evaluate the position of the concrete cavity and could be applied to the non-destructive testing of concrete.

Prospect:
There are still problems in the scope of application as an evaluation technology. However, from a series of inspection results, the algorithm is useful as an evaluation technique for internal defects of concrete structures. In the future, we hope that the proposed algorithm could be employed for in-use concrete structures' non-destructive testing and the quality control and maintenance of prefabricated concrete components products, and the evaluation method can be improved and promoted.

REFERENCES

[1] El-Mesery H S, Mao H, Abomohra A E F. Applications of non-destructive technologies for agricultural and food products quality inspection[J]. Sensors, 2019, 19(4): 846.

[2] Smith A G. Non-destructive testing in industry aviation[J]. Non-Destructive Testing, 1972, 5(3): 170-174.

[3] Schabowicz K. Non-destructive testing of materials in civil engineering[J]. Materials, 2019, 12(19): 3237.

[4] Lu Q Y, Wong C H. Additive manufacturing process monitoring and control by non-destructive testing techniques: challenges and in-process monitoring[J]. Virtual and physical prototyping, 2018, 13(2): 39-48.

[5] Vendan S A, Manoharan S, Nagamani C. MIAB welding of alloy steel tubes in pressure parts: Metallurgical characterization and non destructive testing[J]. Journal of manufacturing processes, 2012, 14(1): 82-88.

[6] Blitz J. Electrical and magnetic methods of non-destructive testing[M]. Springer Science & Business Media, 1997.

[7] Qu Z, Jiang P, Zhang W. Development and application of infrared thermography non-destructive testing techniques[J]. Sensors, 2020, 20(14): 3851.

[8] Usamentiaga R, Venegas P, Guerediaga J, et al. Infrared thermography for temperature measurement and non-destructive testing[J]. Sensors, 2014, 14(7): 12305-12348.

[9] Davis A G, Lim M K, Petersen C G. Rapid and economical evaluation of concrete tunnel linings with impulse response and impulse radar non-destructive methods[J]. NDT & E International, 2005, 38(3): 181-186.

[10] Non-destructive evaluation of reinforced concrete structures: Non-destructive testing methods[M]. Elsevier, 2010.

[11] Merkle T, Meier D, Wagner S, et al. Broadband 240-GHz radar for non-destructive testing of composite materials[J]. IEEE Journal of Solid-State Circuits, 2019, 54(9): 2388-2401.

[12] Bouden T, Nibouche M, Djerfi F, et al. Improving wavelet transform for the impact-echo method of non destructive testing[M]//Future Communication, Computing, Control and Management. Springer, Berlin, Heidelberg, 2012: 241-247.

[13] Zhang R, Olson L D, Seibi A, et al. Improved impact-echo approach for non-destructive testing and evaluation[C]//Proc. 3rd WSEAS Int. Conf. on Advances in Sensors, Signals and Materials. 2010: 139-144.

[14] Carino N J. Impact echo: The fundamentals[C]//Proceedings of the International Symposium Non-Destructive Testing in Civil Engineering (NDT-CE), Berlin, Germany. 2015: 15-17.

[15] Li B, Cao J, Xiao J, et al. Robotic impact-echo non-destructive evaluation based on FFT and SVM[C]//Proceeding of the 11th World Congress on Intelligent Control and Automation. IEEE, 2014: 2854-2859.

[16] Martín-del-Rio J J, Canivell J, Falcon R M. The use of non-destructive testing to evaluate the compressive strength of a lime-stabilised rammed-earth wall: Rebound index and ultrasonic pulse velocity[J]. Construction and Building Materials, 2020, 242: 118060.

[17] Mohammadreza H, Ali S, Hamid S, et al. Application of Schmidt rebound hammer and ultrasonic pulse velocity techniques for structural health monitoring[J]. Scientific Research and Essays, 2012, 7(21): 1997-2001.

[18] Blitz J, Simpson G. Ultrasonic methods of non-destructive testing[M]. Springer Science & Business Media, 1995.

[19] Beard M D, Lowe M J S. Non-destructive testing of rock bolts using guided ultrasonic waves[J]. International journal of rock mechanics and mining sciences, 2003, 40(4): 527-536.

[20] Hassan A M T, Jones S W. Non-destructive testing of ultra high performance fibre reinforced concrete (UHPFRC): A feasibility study for using ultrasonic and resonant frequency testing techniques[J]. Construction and Building Materials, 2012, 35: 361-367.

[21] Le Jeune L, Robert S, Villaverde E L, et al. Plane wave imaging for ultrasonic non-destructive testing: Generalization to multimodal imaging[J]. Ultrasonics, 2016, 64: 128-138.

[22] Febrianti A, Hamdi M, Juandi M. Analysis of non-destructive testing ultrasonic signal for detection of defective materials based on the Simulink Matlab Mathematica computation method[J]. Science, Technology & Communication Journal, 2021, 1(2): 46-58.

[23] Nakamura H, Ohtsu M, Enoki M, et al. Practical acoustic emission testing[M]. Tokyo, Japan:: Springer, 2016.

[24] Su Y, Dong L, Pei Z. Non-Destructive Testing for Cavity Damages in Automated Machines Based on Acoustic Emission Tomography[J]. Sensors, 2022, 22(6): 2201.

[25] Acoustic emission and related non-destructive evaluation techniques in the fracture mechanics of concrete: fundamentals and applications[M]. Woodhead Publishing, 2020.

[26] Schubert, Frank. "Basic principles of acoustic emission tomography." Journal of Acoustic Emission 22.1 (2004): 147-158.

[27] Kobayashi, Y. & T. Shiotani (2012). Seismic tomography with estimation of source location for concrete structures. InStructural Faults and Repair 2012.

[28] Kobayashi, Y., K. Oda, & T. Shiotani (2014). Three-dimensional ae-tomography with accurate source location technique. InStructural Faults and Repair 2014.

[29] Kobayashi Y, Shiotani T. Computerized AE tomography[M]//Innovative AE and NDT Techniques for On-Site Measurement of Concrete and Masonry Structures. Springer, Dordrecht, 2016: 47-68.

[30] Feng, Yiming, et al. " Evaluation of Damage in RC Bridge Decks Reinforced with Steel Plates by AE Tomography." World Conference on Acoustic Emission. Springer, Cham, 2017.

[31] Shiotani, Tomoki, et al. "Visualization of damage in RC bridge deck for bullet trains with AE tomography." Advances in Acoustic Emission Technology. Springer, New York, NY, 2015. 357-368.

[32] Shiotani, Tomoki, et al. " Advanced NDT contributing performance evaluation of civil structures." Asset Intelligence through Integration and Interoperability and Contemporary Vibration Engineering Technologies. Springer, Cham, 2019. 533-543.

[33] Stork, Christof. Ray trace tomographic velocity analysis of surface seismic reflection data. Diss. California Institute of Technol-423 ogy, 1988. 424

[34] Sassa K 1988 Suggested methods for seismic testing within and between boreholes Int. J. Rock Mech. Min. Sci. 25 449–72 425

[35] Tibshirani, Robert. "Regression shrinkage and selection via the lasso." Journal of the Royal Statistical Society: Series B (Method-426 ological) 58.1 (1996): 267-288.

[36] Schubert, Frank. "Basic principles of acoustic emission tomography." Journal of Acoustic Emission 22.1 (2004): 147-158.)

[37] Kobayashi Y. Three-dimensional seismic tomography with tetrahedra element on isoparametric mapping[J]. International Journal of Structural Engineering, 2012, 3(1-2): 37-47.

[38] Kobayashi Y, Shiotani T, Oda K. System identification for three-dimensional AE-tomography with Kalman filter[J]. Proceedings of the 31st European Working Group on Acoustic Emission, Dresden, Germany, 2014: 3-5.

[39] Kobayashi Y, Shiotani T. TWO-DIMENSIONAL Q-VALUE AE-TOMOGRAPHY AND ITS VERIFICATION ON NUMERICAL INVESITIGATIONS[J]. Journal of Acoustic Emission, 2016, 33.

[40] Shiotani T, Nishida T, Nakayama H, et al. Fatigue Failure Evaluation of RC Bridge Deck in Wheel Loading Test by AE Tomography [M]//Advances in Acoustic Emission Technology. Springer, Cham, 2017: 251-264.

[41] He J-H. Application of homotopy perturbation method to nonlinear wave equations. Chaos, Solitons & Fractals. 2005; 26(3):695±700.

[42] He J-H. Variational iteration methodÐsome recent results and new interpretations. Journal of computational and applied mathematics. 2007; 207(1):3±17.

[43] Boyd S, Vandenberghe L. Convex optimization: Cambridge university press; 2004.

[44] A. Bruckstein, D. Donoho, and M. Elad. From sparse solutions of systems of equations to sparse modeling of signals and images. (in press) SIAM Review, 2007.

[45] Jiang B, Zhao W, Wang W. Improved Ultrasonic Computerized Tomography Method for STS (Steel Tube Slab) Structure Based on Compressive Sampling Algorithm. Applied Sciences. 2017; 7(5):432.

[46] He J-H. A tutorial and heuristic review on Lagrange multiplier for optimal problems. Nonlinear Sci Lett A. 2017; 8(2):121±48.

[47] Donoho D L 2006 Compressed sensing IEEE Trans. Inf. Theory 52 1289–306

[48] Emmanuel J. Candès and Michael B. Wakin 2008 An Introduction To Compressive Sampling IEEE Signal Process. Mag. 77 6897–912.

[49] Candès E J, Romberg J and Tao T 2006 Robust uncertainty principles: Exact signal reconstruction from highly incomplete frequency information IEEE Trans. Inf. Theory 52 489–509.

[50] Candès E J, Romberg J K and Tao T 2006 Stable signal recovery from incomplete and inaccurate measurements Commun. Pure Appl. Math. 59 1207–23.

[51] Xin, Q., Yoshikazu, K., Kenichi, O., & Katsuya, N The application of compressive sampling in elastic wave velocity tomography.

[52] Wang, W.; Wang, C.; Bao, Y.; Li, H The study of compressive sampling in ultrasonic computerized tomography. In Proceedings of the 22nd Annual SPIE Smart Structures and Materials + Nondestructive Evaluation and Health Monitoring, San Diego, CA, USA, 8–12 March 2015.

[53] Hashimoto K, Shiotani T, Nishida T and Miyagawa T 2017 Application of elastic-wave tomography to repair inspection in deteriorated concrete structures J. Disaster Res. 12 496–505.

[54] Jiang B, Jia P, Zhao W, Wang W The application of compressive sampling in rapid ultrasonic computerized tomography (UCT) technique of steel tube slab (STS). PloS one. 13 1-15.

[55] Sassa K 1988 Suggested methods for seismic testing within and between boreholes Int. J. Rock Mech. Min. Sci. 25 449–72.

[56] Qiao X, Kobayashi Y, Oda K, et al. verification of elastic wave velocity tomography based on compressive sampling[C]//IOP Conference Series: Materials Science and Engineering. IOP Publishing, 2022, 1242(1): 012032.

[57] Types of damage in concrete structures[M]//Failure, distress and repair of concrete structures. Reference: Kovler K, Chernov V. Woodhead Publishing, 2009: 32-56.

[58] Acoustic emission testing [M]. Springer Science & Business Media, 2008

[59] Shiotani T, Aggelis D G, Makishima O. Global monitoring of large concrete structures using acoustic emission and ultrasonic techniques: case study[J]. Journal of Bridge Engineering, 2009, 14(3): 188-192.

[60] Shiotani T, Ohtsu H, Momoki S, et al. Damage evaluation for concrete bridge deck by means of stress wave techniques[J]. Journal of Bridge Engineering, 2012, 17(6): 847-856.

[61] Shiotani T, Osawa S, Kobayashi Y, et al. Application of 3D AE tomography for triaxial tests of rocky specimens[C]//Proceedings of 31st conference of the European Working Group on Acoustic Emission (EWGAE). 2014.

[62] Sause M G R. Investigation of pencil-lead breaks as acoustic emission sources[J]. 2011.

ACKNOWLEDGMENTS